Sensitivity Study of Energy Transfer Between Mesoscale Eddies and Wind-Induced Near-Inertial Oscillations

Yu Zhang[1], Jintao Gu[1], Shengli Chen[1*], Jianyu Hu[2], Jinyu Sheng[3], Jiuxing Xing[1]

[1]Institute for Ocean Engineering, Shenzhen International Graduate School, Tsinghua University, Shenzhen, 518055, China

[2]State Key Laboratory of Marine Environmental Science, College of Ocean and Earth Sciences, Xiamen University, Xiamen, 361102, China

[3]Department of Oceanography, Dalhousie University, Halifax, NS B3H 4R2, Canada

Correspondence to: Shengli Chen (shenglichen@sz.tsinghua.edu.cn)

Abstract. Analyses of current observations and numerical simulations at two moorings in the northern South China Sea reveal the transfer of near-inertial energy between the background currents associated with mesoscale eddies and near-inertial currents (NICs). A series of numerical experiments are conducted to determine important parameters affecting the energy transfer between idealized mesoscale eddies and NICs generated by rotating winds. Speeds of NICs transferred by both cyclonic and anticyclonic mesoscale eddies increase linearly with the wind stress and eddy strength. The transferred NICs in anticyclonic eddies have current amplitudes of about six times larger than in cyclonic eddies. The translation speed of the mesoscale eddy and the wind rotation frequency also affect the conversion of NICs. The energy transfer rate is elevated with the increase of the positive Okubo-Weiss parameter. A simple theoretical analysis is conducted to verify our findings based on numerical results. Analytical solutions confirm the evident asymmetry of the energy transfer between anticyclonic and cyclonic eddies, and demonstrate quantitatively the relationship between the wind stress and the near-inertial energy transferred by mesoscale eddies.

1 Introduction

Near-inertial oscillations (NIOs) are very common in the global ocean and they appear as a prominent peak in the spectrum of ocean currents (Garrett, 2001). NIOs contain almost half the total kinetic energy of the internal waves and significantly contribute to the vertical shear in the internal waveband (Ferrari & Wunsch, 2009). When surface winds with high spatiotemporal

29 variations act at the ocean surface, strong NIOs could occur in the ocean surface mixed layer (SML,

30 Chen et al., 2015a; D'Asaro et al. 1995; Pollard & Millard, 1970). At the base of the SML, near-

31 inertial internal waves (NIWs) are generated through the horizontal convergence and divergence

32 of the SML (Gill, 1984). These NIWs are free to radiate to the thermocline and deep waters, and

33 low-mode NIWs with long wavelengths can propagate at least hundreds of kilometers toward the

34 equator from their source regions (Alford, 2003; Jochum et al., 2013; Munk & Wunsch, 1998).

35 NIOs not only affect the energy, momentum, and material transport in the upper ocean, but also

36 play an important role in maintaining diapycnal mixing and global ocean circulation (Chen et al.,

37 2016; Greatbatch, 1984; Price et al., 1986; Wunsch & Ferrari, 2004).

38   Due to the turbulent and inhomogeneous nature of the ocean, the central frequency of NIOs

39 is influenced by the β effect and shows a significant blue or red shift induced by the relative

40 vorticity of mesoscale eddies (Chen et al., 2015b; Elipot et al., 2010; Kunze, 1985; Mooers, 1975;

41 Perkins, 1976; Sun et al., 2011). If the magnitude of the gradient in the relative vorticity is larger

42 than the β effect (Chelton et al. 2011), mesoscale eddies also modulate the energy distribution and

43 propagation of the near-inertial motions (van Meurs, 1998; Wang et al., 2024). Previous studies of

44 current observations in the northwestern South China Sea (nSCS) demonstrated that the near-

45 inertial energy propagates both upwards and downwards under the influence of the anticyclonic

46 eddies (Chen et al., 2013; Zhai et al., 2007). Using the in situ observations and ray-tracing

47 techniques, Jaimes and Shay (2010) demonstrated that anticyclonic eddies trap the near-inertial

48 kinetic energy which rapidly propagates vertically below the thermocline and even to the deep

49 ocean. Young and Jelloul (1997) suggested that the anticyclonic eddies can improve the vertical

50 propagation rate of the near-inertial energy by deepening the thermocline. Zhai et al. (2005)

51 demonstrated that the wind generated near-inertial kinetic energy is also high in the strong

52 mesoscale motion regions. Based on the numerical study, Lelong et al. (2020) reveled that

53 anticyclonic eddies facilitate the energy transfer from wind-driven inertial energy to propagating

54 waves. Fer et al. (2018) found that subinertial waves trapped within the Lofoten Basin eddy can

55 significantly contribute to the observed turbulence in the eddy.

56   Mesoscale eddies and NIOs are energetic in the SML (Bühler & McIntyre, 2005; Vanneste,

57 2013; Xie & Vanneste, 2015). Mesoscale eddies not only change the spatial distribution of NIOs,

58 but also exchange the energy with NIOs through the nonlinear interaction (Muller, 1976; Thomas,

59 2012). Based on the observational studies of specific NIO events, Noh and Nam (2020) found that

2

mesoscale eddies can effectively enhance the intensity of NIOs. The energy transfer also occurs between NIOs and low-frequency geostrophic currents through the nonlinear interaction (Liu et al., 2023; Thomas, 2012; Whalen et al., 2020). Jing et al. (2018) demonstrated that the large-scale geostrophic currents of the Gulf Stream affect the distribution of near-inertial energy. Whitt and Thomas (2015) suggested that, in a unidirectional laterally sheared geostrophic flow, a continuous energy transfer occurs between mesoscale eddies and NIOs. In the Kuroshio extension, due to the change of the effective Coriolis frequency caused by the relative vorticity of mesoscale eddies, the energy exchange efficiency between the anticyclonic eddies and NIOs is about twice that between the cyclonic eddies and NIOs (Jing et al., 2017). Based on numerical results in the Icelandic Basin, Barkan et al. (2021) found that a significant energy transfer occurs between NIOs and sub-inertial motions, with the energy transfer rate in winter and summer are about half and a quarter of the local near-inertial wind energy input, respectively. The above and other studies suggested that the energy transfer processes between mesoscale eddies and NIOs should play an important role in the ocean energy cascade (Alford et al., 2016; Ford et al., 2000; McWilliams, 2016; Thomas, 2017). Nevertheless, most of previous studies focused on the energy transfer rate and efficiency. There is a knowledge gap in the amplitude of the near-inertial energy transferred by the mesoscale eddy and the sensitivity of the above-mentioned energy transfer to mesoscale eddies and wind parameters. The main objective of this study is to quantity the energy transfer between the mesoscale eddies and wind-induced NIOs.

This paper is structured as follows. Section 2 provides a brief description of observational data and reanalysis used in this study. Section 3 presents the original and modified slab models. Model results for the energy transfer between mesoscale eddies and the NIOs are given in Sect. 4. A series of sensitivity experiments for determining the important factors affecting the energy transfer is presented in Sect. 5. The results of sensitivity experiments are verified through theoretical analysis in Sect. 6. Summary and discussions are given in Sect. 7.

2 Observational and Reanalysis Data

Current observations at two subsurface moorings named S2 and S3 respectively in the nSCS (marked in Fig. 1) are analyzed here. The current observations at these two moorings were made using the Acoustic Doppler Current Profilers (ADCPs). Mooring S2 is located at 117°39.619′ E and 21°37.001′ N, with the water depth of 499 m. Current observations at this location were made

90 at depth bins from 58 m to 442 m from 22 August 2016 to 8 May 2017. At ADCP mooring S2, the

91 vertical sampling interval is 16 m and the time internal is 60 minutes. ADCP mooring S3 is located

92 at 117°26.528′ E and 21°52.945′ N, with the water depth of 266 m. Current observations at this

93 mooring were made at depth bins from 37 m to 229 m during the same observational period as at

94 location S2. At mooring S3, the vertical sampling interval is 8 m and the time internal is 30 minutes.

95   Hourly winds at 10 m above the mean sea level in the nSCS were extracted from the European

96 Centre for Medium-Range Weather Forecasts (ECMWF) ERA5 reanalysis. The ERA5 winds from

97 July 2016 to June 2017 with an interval of 1 hour and the horizontal resolution of 0.25° are used

98 to calculate the hourly wind stress to be used as the model forcing. The wind speed data obtained

99 from ERA5 is widely used in previous researches on near-inertial motions in the Northwestern

100 Pacific.

101   The surface geostrophic currents used in this study were derived from the sea level grid data

102 provided by the Copernicus Atmosphere Monitoring Service (C3S). The sea surface height

103 anomaly and geostrophic current data in the nSCS from July 2016 to June 2017 are used here,

104 which have a horizontal resolution of 0.25° and a time interval of 24 hours.

105 The mixed layer depth (MLD) for the nSCS was extracted from the 2018 edition of the World

106 Ocean Atlas (WOA2018) (www.ncei.noaa.gov/products/world-ocean-atlas), with a horizontal

107 resolution of 0.25°. The MLD at each location is defined as the depth at which the vertical change

108 of the potential density from the ocean surface is 0.125 (sigma units).
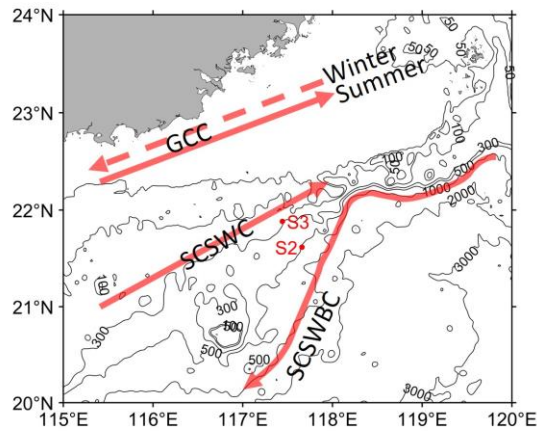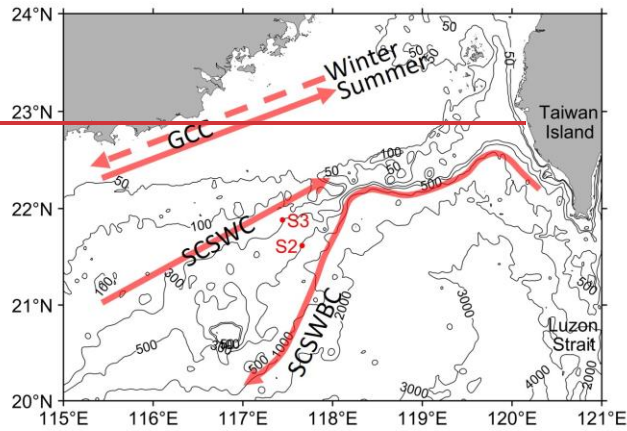
109

4

Figure 1. Major bathymetric feature and circulation (from Shu et al., 2018) of the northern South China Sea. Two red dots represent locations of two ADCP moorings named S2 and S3. Black contours represent isobaths in meter. GCC refers to the Guangdong Coastal Current, SCSWC refers to the South China Sea Warm Current and SCSWBC refers to the South China Sea Western Boundary Current. The solid (dashed) line in the GCC indicates the current direction in summer (winter).

3 Method

3.1 Strain and Vorticity of a Mesoscale Field

The vertical component of the relative vorticity (ζ) has been used to measure the rate of fluid rotation within a mesoscale eddy, which is defined as

$$\zeta = \frac{\partial V}{\partial x} - \frac{\partial U}{\partial y}, \tag{1}$$

where U and V are zonal (eastward) and meridional (northward) surface geostrophic currents, respectively.

The effective Coriolis frequency (f_{eff}) is defined as (Kunze, 1985)

$$f_{eff} = f + \frac{\zeta}{2} \tag{2}$$

where f is the inertial frequency.

The normal and shear components of the rate of strain tensor, S_n and S_s are defined as

$$S_n = \frac{\partial U}{\partial x} - \frac{\partial V}{\partial y}, \tag{3}$$

$$S_s = \frac{\partial V}{\partial x} + \frac{\partial U}{\partial y}. \tag{4}$$

The relative importance of total strain and relative vorticity is diagnosed with the Okubo-Weiss parameter (Okubo 1970):

$$OW = S_n^2 + S_s^2 - \zeta^2. \tag{5}$$

In this study, the dependence of the energy transfer between the mesoscale eddy and NICs on the relative vorticity is considered.

3.2 Modified Slab Model

A simple linear model known as the slab model (Pollard & Millard 1970) was used in simulating NIOs in the SML. Analysis of observed currents in the nSCS (to be discussed in Sect. 4) demonstrates that NIOs can also occur in the SML under nearly steady winds. This suggests the importance of the energy transfer between the background currents and near-inertial currents

142   (NICs). To investigate this energy transfer, the background geostrophic currents (U, V) are added

143   to the original slab model as the modified slab model (Jing et al., 2017; Weller, 1982):

$$\begin{cases} \frac{\partial u}{\partial t} + u\frac{\partial U}{\partial x} + v\frac{\partial U}{\partial y} = fv - ru + \frac{\tau_x}{\rho_o H_{mix}} \\ \frac{\partial v}{\partial t} + u\frac{\partial V}{\partial x} + v\frac{\partial V}{\partial y} = -fu - rv + \frac{\tau_y}{\rho_o H_{mix}} \end{cases} \tag{6}$$

145   where (u,v) are zonal and meridional currents averaged vertically in the SML, and H_{mix} is the

146   MLD. The damping coefficient r is set to 1/8 days^{-1}, which is used to parameterize the loss of near-

147   inertial energy. In Eq. (6), f is the inertial frequency, and ρ_o is the seawater density set to be 1024

148   kg m^{-3}. Wind stress components (τ_x, τ_y) are calculated using ERA5's 10-m winds with the drag

149   coefficient suggested by Oey et al. (2006).

150   The above modified slab model uses two important assumptions: the Rossby number of the

151   geostrophic currents is assumed to be far less than 1, and the horizontal scale of winds to be much

152   larger than that of mesoscale eddies. By ignoring the background geostrophic currents, the above

153   modified slab model becomes the original slab model, which was used in many previous studies

154   of examining the inertial response in the SML (D'Asaro, 1985; Paduan et al. 1989; Pollard &

155   Millard 1970).

156   The modified slab model in Eq. (6) can be solved numerically using an implicit numerical

157   scheme in time to obtain NICs in the SML:

$$\begin{cases} \frac{u^{n+1}-u^n}{\Delta t} + u^{n+1}U_x^{n+1} + v^{n+1}U_y^{n+1} = fv^{n+1} - ru^{n+1} + \frac{\tau_x^{n+1}}{\rho H_{mix}} \\ \frac{v^{n+1}-v^n}{\Delta t} + u^{n+1}V_x^{n+1} + v^{n+1}V_y^{n+1} = -fu^{n+1} - rv^{n+1} + \frac{\tau_y^{n+1}}{\rho H_{mix}} \end{cases} \tag{7}$$

159   where Δt is the time step, which is set to 3600 s in this study, and subscripts x and y in U and V

160   represent partial derivatives. The initial value of the NICs is set to 0. In Eq. (7), variables with

161   superscripts n and $n + 1$ represent their values at time $n\Delta t$ and $(n + 1)\Delta t$, respectively.

162   After merging some terms, the numerical scheme of the modified slab model can be written

163   as

$$\begin{cases} \frac{u^{n+1}-u^n}{\Delta t} + a_1^{n+1}u^{n+1} + b_1^{n+1}v^{n+1} = c_1^{n+1} \\ \frac{v^{n+1}-v^n}{\Delta t} + a_2^{n+1}u^{n+1} + b_2^{n+1}v^{n+1} = c_2^{n+1} \end{cases} \tag{8}$$

165   where $a_1 = U_x + r, a_2 = V_x + f, b_1 = U_y - f, b_2 = V_y + r, c_1 = \tau_x/\rho H_{mix}, c_2 = \tau_y/\rho H_{mix}$.

166   Equation (8) can be written in the following tensor form:

167

$$\begin{bmatrix} a_1^{n+1} + \frac{1}{\Delta t} & b_1^{n+1} \\ a_2^{n+1} & b_2^{n+1} + \frac{1}{\Delta t} \end{bmatrix} \begin{Bmatrix} u^{n+1} \\ v^{n+1} \end{Bmatrix} = \begin{Bmatrix} \frac{u^n}{\Delta t} + c_1^{n+1} \\ \frac{v^n}{\Delta t} + c_2^{n+1} \end{Bmatrix}. \tag{9}$$

168   The numerical update equations for currents are given as

169

$$u^{n+1} = \frac{1 + \Delta t b_2^{n+1}}{(1 + \Delta t a_1^{n+1})(1 + \Delta t b_2^{n+1}) - \Delta t b_1^{n+1} a_2^{n+1}} \left[\frac{u^n}{\Delta t} + c_1^{n+1} - \frac{\Delta t b_1^{n+1}}{1 + \Delta t b_2^{n+1}} \left(\frac{v^n}{\Delta t} + c_2^{n+1} \right) \right], \tag{10}$$

170

$$v^{n+1} = \frac{1 + \Delta t a_1^{n+1}}{(1 + \Delta t a_1^{n+1})(1 + \Delta t b_2^{n+1}) - \Delta t b_1^{n+1} a_2^{n+1}} \left[\frac{u^n}{\Delta t} + c_1^{n+1} - \frac{\Delta t a_2^{n+1}}{1 + \Delta t a_1^{n+1}} \left(\frac{v^n}{\Delta t} + c_2^{n+1} \right) \right]. \tag{11}$$

171 **3.3 Analysis of NICs**

172   The observed zonal and meridional currents at 58.3 m below the sea surface at location S2
173 and at 37.7 m at location S3 (marked in Fig. 1) in the nSCS are analyzed to estimate the near-
174 inertial kinetic energy in the SML. The observed NICs are obtained by using a band-pass filter
175 through Fourier transform with a frequency band of $0.85f$-$1.15f$.

176   The surface geostrophic currents described in Sect. 2 are specified in the modified slab model,
177 based on the assumption that the geostrophic currents are vertically uniform in the SML during
178 the study period. The simulated currents by the original and modified slab models are band-passed
179 through Fourier transform with the frequency band of $0.85f$-$1.15f$ and are further smoothed using
180 a running window of two inertial periods to obtain the simulated amplitude of NICs.

181   To quantitatively assess performances of the original and modified slab models, the
182 correlation analysis and root mean square error (RMSE) analysis between the original slab model,
183 the modified slab model and observations respectively are made.

184 **4 Results**

185 **4.1 Observed NICs**

186   Time series of observed NICs at the top depth bins (58.3 m at S2 and 37.7 m at S3) of two
187 subsurface ADCP moorings (known as $\vec{u}_{S2}^{top}$ and $\vec{u}_{S3}^{top}$) are shown in black lines in Fig. 2 during
188 the observational period from day 234 (22 August 2016) to day 492 (7 May 2017) with respect to
189 1 January 2016. Intense NICs were generated and lasted for about 11 days from day 293 to day

190 304 under the largest wind forcing (~1.6 N m^{-2}) on day 293 (Fig. 2e and 2f). The largest speed of

191 NICs was ~0.30 m s^{-1} on day 295 at the top depth bin at mooring S2 (Fig. 2a) and ~0.37 m s^{-1} on

192 day 296 at the top depth bin at mooring S3 (Fig. 2b). Some NICs were also excited on other days

193 when the winds were relatively weak and nearly steady.
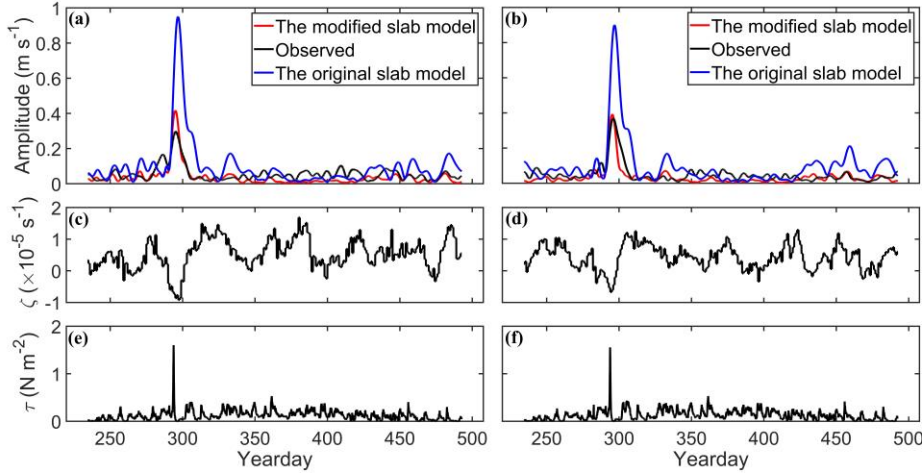
194

195 **Figure 2.** Speeds (m s^{-1}) of observed (black line) and simulated NICs at the top depth bins of
196 ADCP observations at moorings (a) S2 and (b) S3. Red and blue lines denote model results
197 produced by the modified slab and original slab models respectively. Time series of relative
198 vorticity of the surface geostrophic currents at moorings (c) S2 and (d) S3, and time series of wind
199 stress at moorings (e) S2 and (f) S3. The yearday is defined as the number of days elapsed since
200 00:00:00 (GMT) on 1 January 2016.

201

202   Observed NICs at other depth bins of these two ADCP moorings reveal that the intense NICs

203 occurred on days 293-304 at depths between 60 m and 200 m at mooring S2 (not shown) and these

204 NICs were originated from the SML. At mooring S3, similar intense NICs occurred at depths

205 between 40 m and 180 m on days 280-305 (not shown), and these NIC were also originated from

206 the SML. On days 306-318, in comparison, moderate NICs occurred in the lower layer between

207 150 m and 310 m at these two moorings.

208   It should be noted that the current observations ($\vec{u}_{S2}^{top}$ and $\vec{u}_{S3}^{top}$) at the top bins of the two

209 ADCP moorings are in the lower part of the SML or below the SML during the observational

210 period. Based on WOA2018, the climatological monthly mean MLD at the two ADCP moorings

211 is the thinnest and ~20 m in August (days 234-243) and increases to the maximum value of ~90 m

9

212   in January (days 366-396). The MLD decreases from ~56 m in February (days 397-424) to ~37 m

213   in May (days 486-492) and is about 25 m in June and July. This suggests that the observed NICs

214   at the top depth bin (58.3 m) of S2 were made in the lower part of the SML in December and

215   January (days 335-396), but below the SML on the other days of the observational period (Fig.

216   2a). By comparison, the observed NICs at the top depth bin (37.7 m) of S3 were made in the middle

217   of the SML in December and January (days 335-396), and in the lower part of the SML in October

218   and November (days 274-334) and February-May (days 397-492).

219   The relative vorticity estimated from the surface geostrophic currents was negative at the two

220   moorings on days 290-300 (Fig. 2c and 2d), with the maximum negative values of about -0.92×10^{-5}

221   s^{-1} ($-0.17f$) at mooring S2 and about -0.68×10^{-5} s^{-1} ($-0.13f$) at mooring S3. The negative values

222   of the relative vorticity during this period resulted from the westward propagation of an

223   anticyclonic eddy. As shown in Fig. 3a and 3f, moorings S2 and S3 were located over the area

224   between a relatively strong anticyclonic eddy and a weak cyclonic eddy on day 295. The

225   anticyclonic eddy moved westward and passed mooring S2 before day 316 (Fig. 3b and 3g). On

226   day 316, the relative vorticity was low and positive of about 1.23×10^{-5} s^{-1} ($0.23f$) at mooring S2

227   and 0.83×10^{-5} s^{-1} ($0.15f$) at mooring S3 respectively.

228   On days 350-450, an anticyclonic eddy moved southwestward and passed through these two

229   moorings S2 and S3 (Fig. 3c, 3d, 3h, and 3i). There was a week cyclonic eddy close to the two

230   moorings on day 435 (Fig. 3d and 3i). The relative vorticity was relatively strong and positive

231   during this period, with the maximum positive values of about 1.68×10^{-5} s^{-1} ($0.31f$) on day 380 at

232   mooring S2 and 1.29×10^{-5} s^{-1} ($0.24f$) on day 423 at mooring S3 respectively.

233   Between days 451-492, there is a week anticyclonic eddy close to the moorings S2 and S3

234   and the two moorings are located at the edge of the anticyclonic eddy on day 452 (Fig. 3e and 3j).
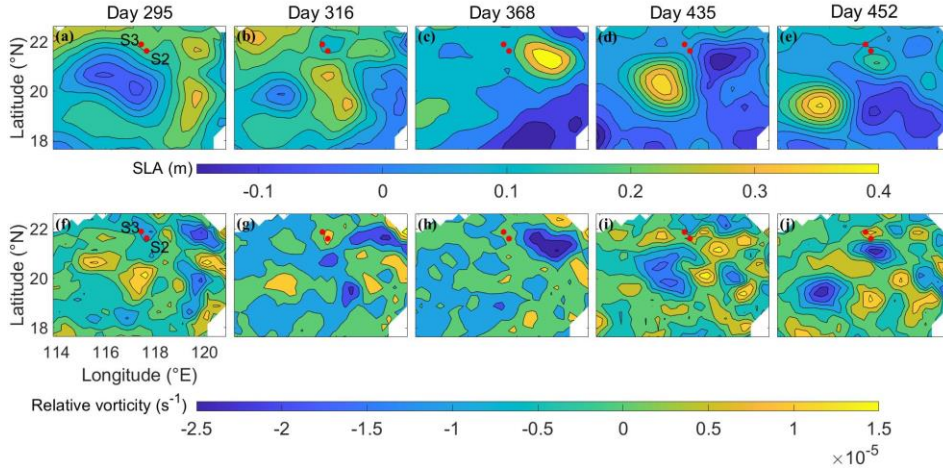
235

Figure 3. Spatial distributions of sea surface level anomaly (SLA) on day 295 (a), day 316 (b), day 368 (c), day 435 (d) and day 452 (e). Spatial distributions of the relative vorticity on day 295 (f), day 316 (g), day 368 (h), day 435 (i) and day 452 (j). Two red dots mark locations of two ADCP moorings S2 and S3.

4.2 Simulated NICs

Numerical simulations are made using the original and modified slab models to examine whether the energy exchange occurs between the mesoscale eddy and NICs in the SML at moorings S2 and S3. Both the original and modified slab models assume that the NICs in the SML is vertically uniform and use the damping coefficient r set to a relatively small value of 1/8 day^{-1}. Both the models are forced by time series of wind stress shown in Fig. 2e and 2f.

The simulated NICs produced by the original slab model at the top bins of two ADCP moorings are shown by the blue lines in Fig. 2a and 2b. The simulated NICs by the original slab model are large and about 0.95 m s^{-1} (0.90 m s^{-1}) at mooring S2 (S3) on day 296 and relatively weak on days 350-430. In comparison with the observed NICs, the original slab model has large deficiency of overpredicting significantly the observed large NICs on days 285-300 at the two stations and also overpredicting moderately the observed NICs on other days of the observational period. It should be noted that the results of both the original and modified slab models using three different damping coefficients (r = 1/5 day^{-1}, 1/6 day^{-1} and 1/7 day^{-1}) and annual mean MLD at

11

255   two stations (~45 m) are highly similar with the model results using $r = 1/8$ day^{-1} and monthly
256   mean MLD shown in Fig. 2a and 2b.

257   In comparison with the original slab model results, the modified slab model generates much
258   smaller NICs than the original slab model on days 280-305 (red lines in Fig. 2a and 2b), with the
259   maximum value of about 0.42 m s^{-1} at mooring S2 and about 0.39 m s^{-1} at mooring S3 on day 295.
260   In comparison with the observed NICs at the two moorings, the modified slab model performs
261   significantly better than the original slab model on days 250-325 and days 451-492, indicating the
262   importance of the energy exchange between the background mesoscale eddies and NICs. On days
263   350-450, the relative vorticity of the background currents is positive, which results in the simulated
264   NICs produced by the modified slab model to be slightly weaker than the observed NICs at these
265   two moorings. As mentioned in Sect. 4.1, the top depth bins of the ADCP observations at the two
266   moorings were in the lower part of the SML or below the SML during the observational period,
267   which explains partially the differences between observed and simulated NICs by the modified
268   slab model shown in Fig. 2a and 2b. Differences between the observed and simulated NICs can
269   also partially be explained by the assumption of vertically uniform geostrophic currents in the
270   SML and exclusion of baroclinic dynamics.

271   The above analysis based on results shown in Fig. 2 suggests that, overall, the simulated NICs
272   produced by the modified slab model agree with the observed NICs significantly better than the
273   original slab model at two moorings S2 and S3. This indicates the occurrence of the near-inertial
274   energy transfer induced by the interaction between mesoscale eddies and NICs in the SML during
275   the observational period.

276   To quantify the model performance, we use the correlation coefficient (R) and the root mean
277   square error (RMSE) based on the time series of observed and simulated NICs shown in Fig. 2a
278   and 2b. The modified slab model has a higher correlation coefficient (R = ~0.81) and smaller root
279   mean square error (RMSE = ~0.04 m s^{-1}) than the original slab model (R = ~0.70 and RMSE =
280   ~0.12 m s^{-1}) at mooring S2. At mooring S3, the R value between the observed NICs and results of
281   the modified slab model is ~0.84, and RMSE is ~0.03 m s^{-1}. For the original slab model at location
282   S3, the R value is ~0.85, and RMSE is ~0.10 m s^{-1}. These statistical indices suggest that the
283   modified slab model performs better than the original slab model, especially in reproducing the
284   amplitude of the observed NICs. This also suggests the energy transfer between mesoscale eddies

12

285 and NICs may be a non-negligible process in the energy cascade across different scales in the
286 global ocean.

287

288

289 **Table 1.** Correlation coefficients (R) and RMSEs between the simulation results of the modified
290 and original slab models and observations for the observational period, respectively.

Mooring	Correlation coefficient (R)		RMSE (m s^{-1})	
	Original slab model	Modified slab model	Original slab model	Modified slab model
S2	0.70	0.81	0.12	0.04
S3	0.85	0.84	0.10	0.03

291 **5 Sensitivity Study**

292   A series of numerical experiments (in total 226) are conducted using the original and modified
293 slab models to examine sensitivity of model results to the wind speed, the wind rotation frequency,
294 the translational speed of the mesoscale eddy, and the strength of the mesoscale eddy. Both the
295 cyclonic and anticyclonic eddies with an idealized eddy structure are used for simplicity. Results
296 of the original and modified slab models are both band-pass ($0.60f$-$1.40f$) filtered to get broad
297 NICs signals and then smoothed using a running window of two inertial periods to obtain the near-
298 inertial velocity in the SML.

299 **5.1 Idealized Mesoscale Eddy Structure**

300   Based on the composite analysis of satellite altimetry and Argo float data, Zhang et al. (2013)
301 suggested a universal structure of mesoscale eddies in the global ocean. Their universal structure
302 of mesoscale eddies is used in our experiments.

303   The normalized structure $\tilde{P}(\tilde{r}, z)$ of the pressure anomaly in the universal mesoscale eddy
304 used in this study is decomposed into a radial function $R(\tilde{r})$ and a vertical function $H(z)$:

$$\tilde{P}(\tilde{r}, z) = R(\tilde{r}) \, H(z), \tag{12}$$

$$R(\tilde{r}) = \left(1 - \frac{\tilde{r}^2}{2}\right) e^{-\frac{\tilde{r}^2}{2}}, \tag{13}$$

$$H(z_s) = H_0 \sin(k z_s + \theta_0) + H_{ave}, \tag{14}$$

$$\tilde{r} = \frac{r}{R_0}, \tag{15}$$

13

309
$$z_s = \int_0^z \left(\frac{N}{f}\right) dz, \tag{16}$$

where r is the radial distance to the eddy center, R_0 is the radius of the mesoscale eddy, N is the buoyancy frequency, H_0, k, θ_0 and H_{ave} are undetermined coefficients, e.g. in this study, $H_0 = 2/3$，$H_{ave} = 2/3$，$N = 10^{-3}$ $(1/s)$，$k = \pi/18000$，$f = 5 \times 10^{-5}$ (rad/s) and $\theta_0 = \pi/6$. The vertical structure function $H(z)$ defined above is similar with the structural diagram in Zhang et al. (2013).

The structure function for the idealized mesoscale eddy in the Cartesian coordinate system can be written as

$$\tilde{P}(x,y,z) = \left(1 - \frac{x^2+y^2}{2R_0^2}\right) \cdot e^{-\frac{x^2+y^2}{2R_0^2}} \cdot \left[\frac{2}{3} \cdot \sin\left(\frac{\pi}{900} \cdot z + \frac{\pi}{6}\right) + \frac{2}{3}\right], \tag{17}$$

with the origin of the coordinate to be the eddy center at the sea surface.

Using the pressure anomaly suggested by Wei et al. (2017), the equation for the pressure field based on the different strength of mesoscale eddies can be given as

$$P(x,y,z) = P_0 \cdot \tilde{P}(x,y,z) + \bar{P}(z), \tag{18}$$

$$P_0 = g \cdot \rho_0 \cdot SLA_c, \tag{19}$$

where P_0 is the strength of mesoscale eddies，ρ_0 is the reference density of seawater taken as 1024 kg/m³ , g is the gravitational acceleration set to be 9.8 m/s², SLA_c is the sea surface level anomaly (SLA) of the eddy center where the anticyclone eddies are specified as negative values and the cyclonic eddies are positive values, and the average pressure field is denoted by $\bar{P}$. As only mesoscale eddy signals are added to the ocean in this study, $\bar{P}$ is a function of the vertical direction that is homogeneous in the horizontal direction.

Using the geostrophic balance, the zonal and meridional components of the geostrophic velocity at the ocean surface are given as

$$u = -\frac{1}{\rho_0 f}\frac{\partial P}{\partial y} = -\frac{P_0}{\rho_0 f}\left[\frac{y^3+yx^2-4yR_0^2}{2R_0^4}\right] e^{-\frac{x^2+y^2}{2R_0^2}}, \tag{20}$$

$$v = \frac{1}{\rho_0 f}\frac{\partial P}{\partial x} = \frac{P_0}{\rho_0 f}\left[\frac{x^3+xy^2-4xR_0^2}{2R_0^4}\right] e^{-\frac{x^2+y^2}{2R_0^2}}. \tag{21}$$

In this study, the cyclonic and anticyclonic eddies are set to have the same strength with the opposite relative vorticity. Numerical experiments are conducted with the idealized mesoscale eddy moving westward. Figure 4 shows currents and relative vorticity at the sea surface for an

14

idealized anticyclonic eddy with the radius of 120 km, R_0 to be 120 kilometers, P_0 of 6400 kg/m ·

s^2 (i.e., SLA_c is equal to 0.64 m), and the core Rossby number of about -0.7. Based on Eq. (19),

the mesoscale eddy strength P_0 is a positive proportional function of the SLA_c under the constant

seawater density and gravitational acceleration. The strength of the mesoscale eddy can be

characterized by the absolute values of the SLA_c ($|SLA_c|$).

To examine model results inside the eddy, nine fixed locations in space named P1-P9 along

the y-axis (marked in Fig. 4c) are selected. The distance from the eddy center to P1 (P9) is $0.92R_0$,

to P2 (P8) is $0.69R_0$, to P3 (P7) is $0.46R_0$, and to P4 (P6) is $0.23R_0$. After the wind-driven currents

reach a steady state, the mesoscale eddy propagates westward to reach the area of interest (P1-P9).

The zonal and meridional components of currents for an anticyclonic eddy increase from the center

to the edge of the eddy, and then gradually decrease outside the anticyclonic eddy (Fig. 4a and 4b).

The relative vorticity is largest at the eddy center and then reduces gradually from the center to the

edge of the eddy (Fig. 4c). The idealized eddy exhibits a circular positive (negative) vorticity

around the periphery of the idealized anticyclonic (cyclonic) eddy in the Northern Hemisphere
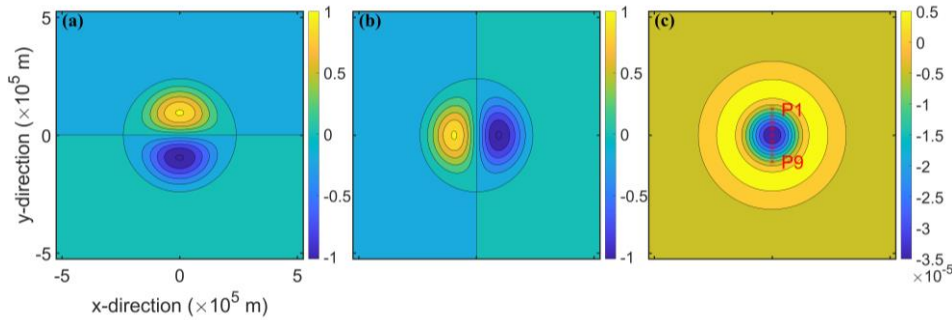
(Zhang et.al 2013).

Figure 4. Distributions of (a) zonal (*u*) and (b) meridional (*v*) components (m s^{-1}) of currents and
(c) relative vorticity (s^{-1}) for an idealized anticyclonic eddy with of radius of 120 km. Model results
at nine fixed locations (P1-P9) denoted by red asterisks along the y-axis in (c) are examined.

带格式的: 行距: 单倍行距

359   Jing et al. (2017) proposed a method to calculate the efficiency of energy transfer from
360   background mesoscale eddies to wind-induced NICs. In this study, we use the differences in the
361   average speeds of NICs between the modified and original model (NICs_U_{AE} and NICs_U_{CE}) as
362   the proxies for the near-inertial energy generated in the mesoscale eddies by the interaction
363   between mesoscale eddies and NICs:

364
$$NICs\_U_{AE} = NICs\_U_{AE}^{Modified} - NICs\_U_{AE}^{Original}, \qquad (22)$$

365
$$NICs\_U_{CE} = NICs\_U_{CE}^{Modified} - NICs\_U_{CE}^{Original}, \qquad (23)$$

366   where $NICs\_U_{AE}^{Modified}$ ($NICs\_U_{AE}^{Original}$) and $NICs\_U_{CE}^{Modified}$ ($NICs\_U_{CE}^{Original}$) are the averaged
367   speeds of NICs based on results produced by the modified (original) slab model in the anticyclonic
368   eddies and cyclonic eddies over the same time period, respectively. It should be noted that the
369   simulated NICs by the original slab model represent the near-inertial energy generated directly by
370   the wind forcing. Therefore, after removing the generation of wind-induced NICs, the differences
371    $NICs\_U_{AE}$ and $NICs\_U_{CE}$ represent the amplitudes of NICs transferred by interactions between
372   mesoscale eddies and NICs in the anticyclonic eddies and the cyclonic eddies respectively.

373   To quantify differences in the NICs transferred by background currents between the
374   anticyclonic and cyclonic eddies, we introduce a simple parameter α, defined as

375
$$\alpha = \frac{NICs\_U_{AE}}{NICs\_U_{CE}}. \qquad (24)$$

376   If α is larger than 1, it means that the anticyclonic eddy can transfer more NICs than the cyclonic
377   eddy with the same strength.

5.2 Effect of Wind Speeds

379   The wind speed affects the energy input from the wind to the SML, and therefore influences
380   interaction between mesoscale eddies and NICs. To facilitate theoretical analysis and generate a
381   reasonable magnitude of the NICs speeds, we conduct the numerical experiments using
382   cyclonically rotating winds and anticyclonically rotating and in the Northern Hemisphere with the
383   constant wind speed (A). The wind stress τ used in our sensitivity study takes a form as follows

384
$$\tau_x(t) + i\,\tau_y(t) = A\,e^{iBt}, \qquad (25)$$

385   where $\tau_x(t)$ and $\tau_y(t)$ are time-dependent zonal and meridional components of wind stress, and

386　*B* is the wind rotation frequency. Positive wind rotation frequencies represent cyclonically
387　rotating winds and negative wind rotation frequencies indicate anticyclonically rotating winds.

388　　　　Five numerical experiments (ExpA1-5) are conducted with the background idealized
389　mesoscale eddy moving westward with a translational speed of 8 cm s^{-1}. The $|SLA_c|$ of both
390　anticyclonic and cyclonic eddies are set to 0.64 m in these five experiments. ~~~~The integration
391　duration of the numerical simulations is 3000 hours. The speeds (A) of time-varying winds in these
392　five experiments are set to 5 m s^{-1}, 10 m s^{-1}, 13 m s^{-1}, 15 m s^{-1}, and 20 m s^{-1} respectively,
393　corresponding to wind stress amplitudes of 0.038 N m^{-2}, 0.150 N m^{-2}, 0.282 N m^{-2}, 0.412 N m^{-2},
394　and 0.876 N m^{-2} respectively. The wind forcing rotates cyclonically at the inertial frequency f.
395　The conclusions drawn from the average and the sum of nine locations (P1-P9) are consistent.~~.~~
396　~~The magnitude of the sum is larger than that of the average, which makes the presentation of the~~
397　~~results clearer and more intuitive.~~

398　　　　For a cyclonic eddy with $|SLA_c|$ = 0.64 m, the ~~sum of~~ averaged speeds of NICs converted
399　from this cyclonic eddy at the above-mentioned nine locations ($NICs\_U_{CE}$ ~~$\sum NICs\_U_{CE}$~~) are about
400　~~1~~0.009~~01$\times$10^{-3}~~ m s^{-1} and 2.32$\times$10^{-2} m ~~0.209 m~~ s^{-1} for cyclonic wind speeds of 5 m s^{-1} (i.e. 0.038
401　N m^{-2}) and 20 m s^{-1} (i.e. 0.876 N m^{-2}) respectively (Fig. 5a). This suggests that, within the cyclonic
402　eddy, the $NICs\_U_{CE}$ ~~$\sum NICs\_U_{CE}$~~ increases 23 times if the cyclonic wind stress increases 23 times,
403　which is consistent with the conclusion based on the analytical solution in Sect. 6.

404　　　　In an anticyclonic eddy with the same strength of $|SLA_c|$ = 0.64 m, the ~~sum of~~ averaged
405　speeds of NICs transferred from this anticyclonic eddy at the nine locations
406　($NICs\_U_{AE}$ ~~$\sum NICs\_U_{AE}$~~) also increases with the wind speeds. The $NICs\_U_{AE}$ ~~$\sum NICs\_U_{AE}$~~ values
407　are about 2.10$\times$10^{-3}~~0.019~~ m s^{-1} and 4.85$\times$10^{-2}~~0.437~~ m s^{-1} for the cyclonic wind speeds of 5 m s^{-1}
408　(corresponding to 0.038 N m^{-2}) and 20 m s^{-1} (corresponding to 0.876 N m^{-2}) respectively (Fig. 5a).
409　This indicates that the averaged speeds of NICs generated in anticyclonic eddies by the interaction
410　between background anticyclonic eddies and NICs also increase linearly with the cyclonic wind
411　stress. But the NICs are stronger in the anticyclonic eddy than in the cyclonic eddy under the same
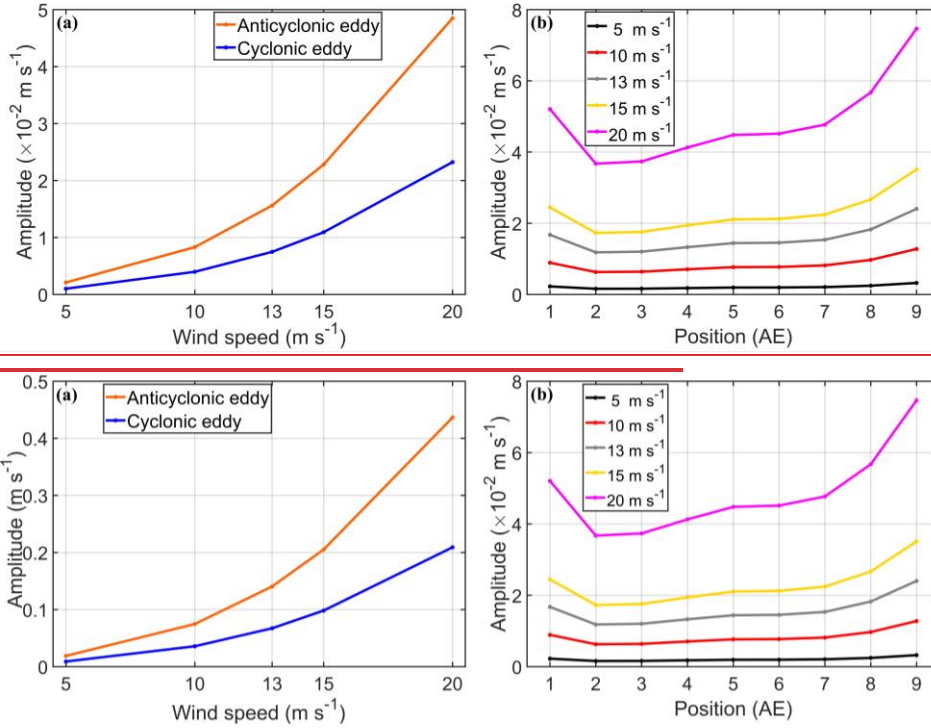412　wind conditions.

413

414

415

Figure 5. (a) ~~Sum of a~~Averaged speeds of transferred NICs at 9 fixed locations P1-P9 as a function of the wind speeds in the anticyclonic eddy (orange line) and cyclonic eddy (blue line), respectively. (b) Averaged speeds of transferred NICs as a function of the wind speeds in the anticyclonic eddy. The black, red, gray, yellow and purple line indicate respectively the wind speed of 5 m s^{-1} (ExpA1), 10 m s^{-1} (ExpA2), 13 m s^{-1} (ExpA3), 15 m s^{-1} (ExpA4) and 20 m s^{-1} (ExpA5). Numbers on the horizontal axis in (b) denote nine fixed locations P1 to P9. The wind rotates cyclonically at the inertial frequency. Mesoscale eddies move westward at the translational speed of 8 cm s^{-1} and $|SLA_c| = 0.64$ m.

It should be noted that, however, the transferred near-inertial energy varies with the actual locations within the mesoscale eddy. We take the example of anticyclonic eddies to illustrate this issue. In anticyclonic eddies, the difference between nine locations P1-P9 is large (Fig. 5b). The amplitude shows a distribution characterized by small values at the eddy center and relatively large values at the eddy edge, and this distribution characteristic is more obvious with the increase of

18

430   the wind speed. The amplitudes of transferred NICs decrease outward from the eddy edge and are
431   small in the rim of the mesoscale eddy.

432   The Okubo-Weiss parameter increases radially outward from the center of the mesoscale
433   eddy. When the wind speed is relatively small, the difference of the energy generation induced by
434   the Okubo-Weiss parameter is not significant (Fig. 5b). With the increase of the wind energy input,
435   the larger absolute value of the positive Okubo-Weiss parameter gradually has the decisive
436   function in the energy transfer. Therefore, it makes the anticyclonic eddy exhibit superior energy
437   conversion characteristics at the eddy edge, which is consistent with the conclusion based on the
438   energy transfer rate (Fig. 10).

439   The α values (Eq. (24)) are about 2.08 based on the ~~sum of~~ averaged speeds of NICs at the
440   nine locations in the five different wind speeds. This indicates that the anticyclonic eddy is more
441   efficient than the cyclonic eddy in transferring the kinetic energy to NICs (Fig. 5a). The difference
442   in the near-inertial energy transfer efficiency between anticyclonic and cyclonic eddies is not
443   affected very much by magnitudes of wind speeds.

444   **5.3 Effect of Wind Rotation Frequencies**

445   The rotation frequency of the winds can affect the generation of the NICs and thus the energy
446   transfer between the mesoscale eddy and NICs, therefore 28 numerical experiments using different
447   wind rotation frequencies ($\pm1.5f$, $\pm1.25f$, $\pm1.2f$, $\pm1.15f$, $\pm1.1f$, $\pm1.05f$, $\pm f$, $\pm0.95f$, $\pm$
448    $0.9f$, $\pm0.85f$, $\pm0.8f$, $\pm0.75f$, $\pm0.5f$ and $\pm0.25f$, where f is the inertial frequency), denoted
449   as ExpB1-28, are conducted. Positive wind rotation frequencies correspond to cyclonically rotating
450   winds, and negative wind rotation frequencies are for anticyclonically rotating winds. In these 28
451   experiments, the mesoscale eddy moves westward at the speed of 8 cm s^{-1} and $|SLA_c|$ = 0.64 m.
452   The winds rotate at different frequencies and the wind speed is set to 13 m s^{-1}.

453   Figure 6 shows the ~~sum of~~ averaged speeds of the transferred NICs at the nine locations as
454   function of the wind rotation frequency for the cyclonic and anticyclonic eddies. Under
455   cyclonically rotating and anticyclonically rotating wind conditions, there is bidirectional energy
456   transfer between mesoscale eddies and NICs. The closer the absolute value of the wind rotation
457   frequency to f, the stronger the energy transfer between mesoscale eddies and NICs. When the
458   wind rotation frequency is negative, the wind rotation direction is the same as that of the local
459   NICs. Wind rotation frequencies close to the inertial frequency of $-f$ can lead to the resonance and

19

induce large NICs. Therefore, the strong NICs provide a significant energy source for reverse energy conversion, allowing the near-inertial kinetic energy to be reabsorbed into the background mesoscale eddies and contribute to the reconstruction of the geostrophic balance.

For cyclonic eddies, the ~~sum of~~ averaged speeds of NICs ($NICs\_U_{CE}$ ~~∑ NICs_U_{CE}~~) is sensitive to the wind rotation frequency. The $NICs\_U_{CE}$ ~~∑ NICs_U_{CE}~~ values are less than zero when the winds rotate cyclonically at the frequencies of $0.25f$, $0.75f$ and $1.25f$ (Fig. 6b) and the winds rotate anticyclonically at frequencies ranging from $-1.15f$ to $-0.75f$ (Fig. 6a), indicating that direction of the energy transfer is from the NICs to the cyclonic eddies. The amplitudes of the energy transferred from NICs to cyclonic eddies under anticyclonically rotating wind conditions are larger than those transferred under cyclonically rotating wind conditions. The addition of mesoscale eddies has a damping effect for NICs, leading to the negative energy transfer that aligns with the observed results (Fig. 2). When the direction of the energy transfer is positive, the $NICs\_U_{CE}$ ~~∑ NICs_U_{CE}~~ has a maximum value of about 7.05×10^{-2}~~0.635~~ m s^{-1} when the winds rotate anticyclonically at the frequency of $-1.25f$.

For anticyclonic eddies, the ~~sum of~~ averaged speeds of NICs ($NICs\_U_{AE}$ ~~∑ NICs_U_{AE}~~) also varies with the wind rotating frequency. When the winds rotate anticyclonically at frequencies ranging from $-1.5f$ to $-0.9f$, the direction of the energy transfer is from NICs to anticyclonic eddies (Fig. 6a). The negative energy transfer is strongest at the resonance frequency of $-f$. The $NICs\_U_{AE}$ ~~∑ NICs_U_{AE}~~ values are all positive under cyclonically rotating winds, which represent the energy transfer from the anticyclonic eddies to NICs (Fig. 6b). The $NICs\_U_{AE}$ ~~∑ NICs_U_{AE}~~ values for the anticyclonic eddies increases from the value of ~2.49~~0.002~~$\times10^{-4}$ m s^{-1} at the wind rotating frequency of $0.25f$ to the maximum value of $\sim2.37\times10^{-2}$~~0.213~~ m s^{-1} at the wind rotating frequency of $0.90f$. The $NICs\_U_{AE}$ ~~∑ NICs_U_{AE}~~ values are larger than the $NICs\_U_{CE}$ ~~∑ NICs_U_{CE}~~ values under the same positive wind rotation frequency. The closer the rotational frequency of the cyclonic winds is to the inertial frequency, the greater the difference in near-inertial energy conversion induced by anticyclonic eddies and cyclonic eddies.
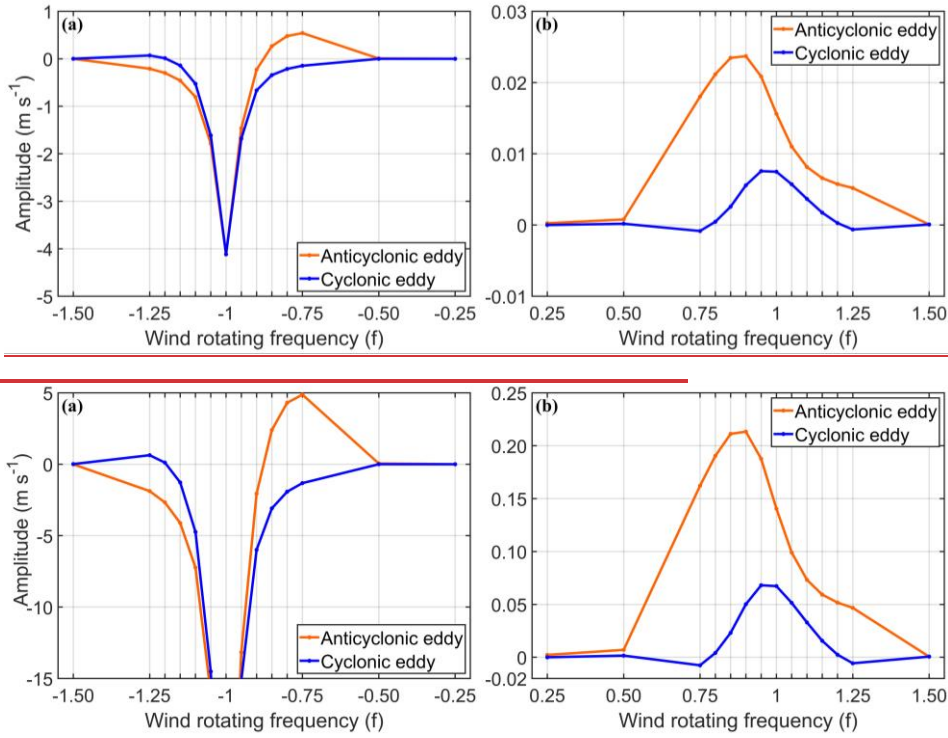
Figure 6. ~~Sum of a~~Averaged speeds of transferred NICs at 9 fixed locations P1-P9 as a function of rotation frequencies of (a) anticyclonically rotating winds and (b) cyclonically rotating winds. The orange and blue line indicate respectively the anticyclonic eddy and cyclonic eddy. The wind rotation frequencies are normalized by the inertial frequency f.

5.4 Effect of Eddy Translational Speeds

The translational speed of a background mesoscale eddy defines the forcing duration of winds and thus the energy input to NICs in the ocean SML. Based on the observations of mesoscale eddies in the nSCS, nine numerical experiments (ExpC1-9) using different translational speeds of mesoscale eddies (4 cm s^{-1}, 5 cm s^{-1}, 6 cm s^{-1}, 7 cm s^{-1}, 8 cm s^{-1}, 9 cm s^{-1}, 10 cm s^{-1}, 11 cm s^{-1}, and 12 cm s^{-1}) are conducted. In these nine experiments, the speed of cyclonically rotating winds at the inertial frequency is set to 13 m s^{-1}. The mesoscale eddy moves westward and $|SLA_c| = 0.64$ m.

21

For the anticyclonic eddy with $|SLA_c| = 0.64$ m, the ~~sum of~~ average speeds of the converted NICs at the nine locations ($NICs\_U_{AE}$ ~~$\sum NICs\_U_{AE}$~~) increases from about ~~0.133~~ 1.48×10^{-2} m s^{-1} to 1.64×10^{-2} ~~0.148~~ m s^{-1} as the translational speeds increase from 4 cm s^{-1} to 11 cm s^{-1} (Fig. 7a). After the translational speed reaches 11 cm/s, the value of $NICs\_U_{AE}$ ~~$\sum NICs\_U_{AE}$~~ remains almost the same as that at a translational speed of 11 cm/s. The increase of the translational speed enhances the total kinetic energy of mesoscale eddies, which can provide a larger energy source and be more beneficial for the conversion of NICs. The translational speed of the mesoscale eddy is smaller than the maximum rotation speed of the mesoscale eddy, which is about 1.62 m s^{-1} in this study. It should be noted that the change in the eddy kinetic energy caused by the different translational speeds is relatively small in comparison with the total eddy energy determined by the mesoscale eddy strength. Therefore, the change in the amplitude of the transferred NICs is relatively small.

For a cyclonic eddy with $|SLA_c| = 0.64$ m, the ~~sum of~~ average speeds of the transferred NICs at the nine locations ($NICs\_U_{CE}$ ~~$\sum NICs\_U_{CE}$~~) range from 7.34×10^{-3} m ~~0.066 m~~ s^{-1} to 7.63×10^{-3} m ~~0.069 m~~ s^{-1} and are not sensitive to the translational speeds (Fig. 7a). Same as in the anticyclonic eddy case, more total kinetic energy is available for generating NICs within the cyclonic eddy with the same structure but with the faster translational speeds. Different from the anticyclonic eddy case, however, the cyclonic eddy is not conducive to the energy transfer to NICs naturally. Therefore, the slightly larger energy source caused by the increase of the translational speeds has little influence on the total amount of kinetic energy transferred from the cyclonic eddy to NICs.

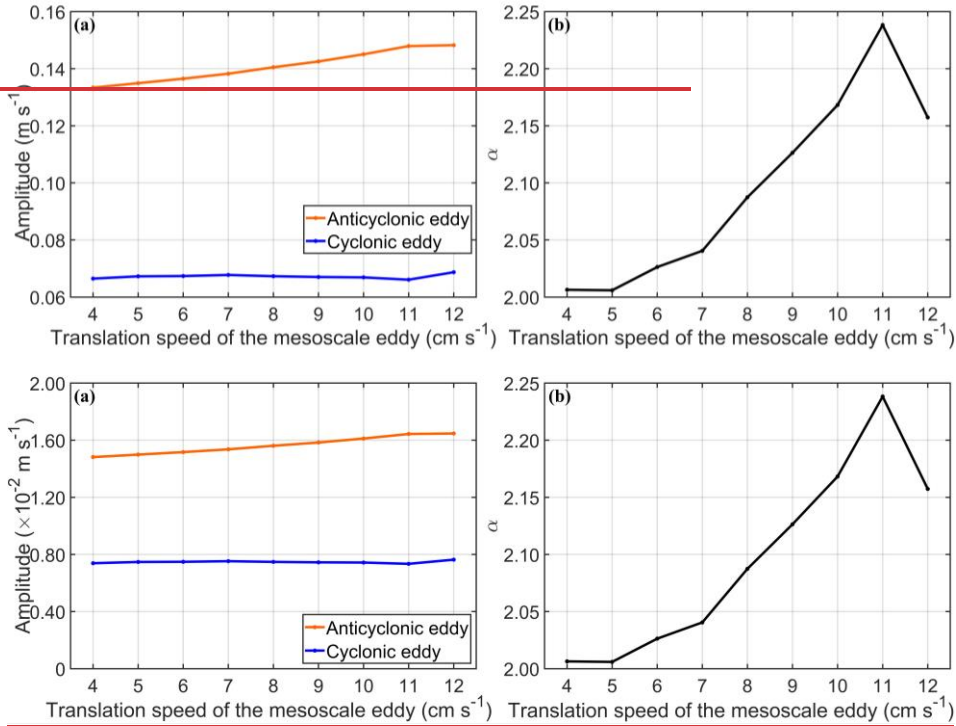**Figure 7.** (a) ~~Sum of a~~Averaged speeds of transferred NICs at 9 fixed locations P1-P9 as a function of the eddy translational speed in the anticyclonic eddy (orange line) and cyclonic eddy (blue line), respectively. (b) The α value as a function of the eddy translational speed. The speed of the cyclonic wind is 13 m s^{-1}, and the wind rotates at the inertial frequency. Mesoscale eddies move westward and $|SLA_c| = 0.64$ m.

The α value has a maximum value of ~2.24 occurring at the eddy translational speeds of 11 cm s^{-1} (Fig. 7b). This means that the anticyclonic eddy transfers much more near-inertial energy than the cyclonic eddy does, particular at the translational speed of 11 cm s^{-1}. After exceeding the translational speed of 11 cm s^{-1}, the α values decrease with the increase of the eddy translational speeds. The α value is ~2.16 at the translational speed of 12 cm s^{-1}. The average speeds of the NICs at the mesoscale eddy edge are generally larger than that of at the mesoscale eddy center.

537   A natural question raises whether the variations of α values within the mesoscale eddy are
538 affected by the strength of anticyclonic eddies. To address this issue, we consider the ~~sum of~~
539 averaged speeds of NICs at nine locations for mesoscale eddies and the α values with different
540 strengths and translational speeds (Fig. 8). We consider the case with the cyclonically rotating
541 wind speed of 13 m s^{-1} at the inertial frequency. For mesoscale eddies with larger $|SLA_c|$ values,
542 the α values are relatively less sensitive to the translational speed. For mesoscale eddies with
543 different $|SLA_c|$ values, the α values all have the maximum values with the translational speeds of
544 11 cm s^{-1}. The α value decreases with the elevated translational speed when the eddy translational
545 speed is larger than 11 cm s^{-1}.
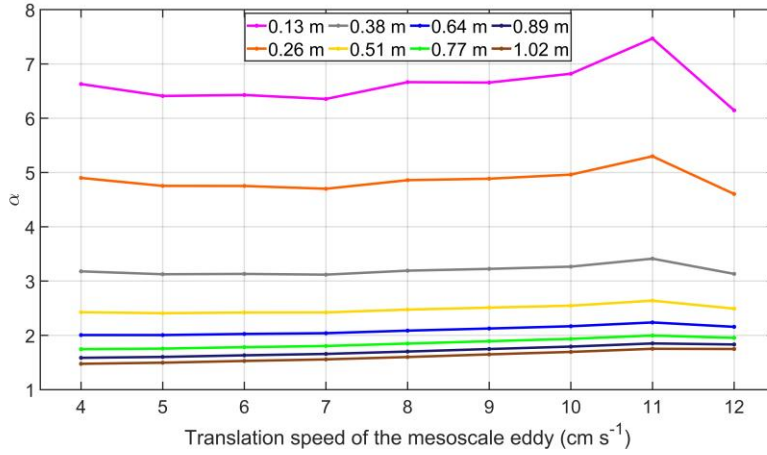
546

547 **Figure 8.** The α values at 9 fixed locations P1-P9 as a function of the strengths and translational
548 speeds of the mesoscale eddies. The speed of the cyclonically rotating winds at the inertial
549 frequency is 13 m s^{-1}. Mesoscale eddies move westward. Different colors of lines represent
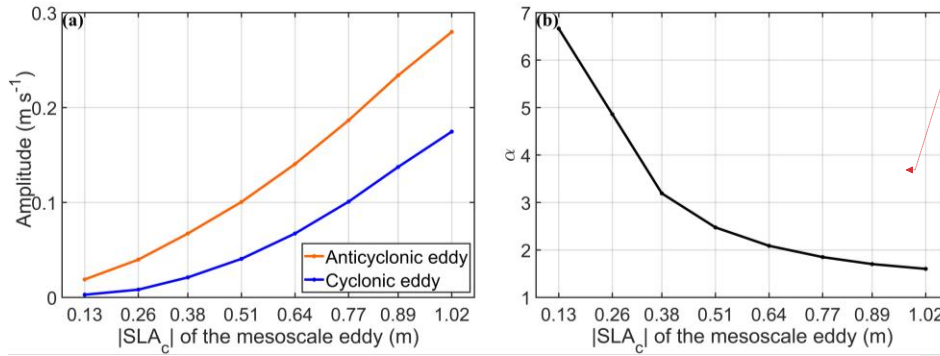550 different mesoscale eddy strengths.

551

5.5 Effect of Mesoscale Eddy Strengths

553   In addition to the effect of the eddy translational speed, other characteristics of mesoscale
554 eddies such as the radius and strength of mesoscale eddies can also affect the energy exchange.
555 Sixteen numerical experiments (denoted as ExpD1-16) are conducted in this section using various
556 strengths of mesoscale eddies. In these sixteen experiments, the speed of cyclonically rotating

24

wints at the inertial frequency is set to 13 m s^{-1}, the translational speed of mesoscale eddies is set to 8 cm s^{-1}, and the eddy translational direction to be westward. The $|SLA_c|$ ~~$|SLA_c|$~~ values are set to 0.13 m, 0.26 m, 0.38 m, 0.51 m, 0.64 m, 0.77 m, 0.89 m, and 1.02 m for cyclonic and anticyclonic eddies, respectively.

Figure 9a shows that the ~~sum of~~ averaged speeds of the transferred NICs at nine locations as a function of the mesoscale eddy strengths for the cyclonic eddies ($NICs\_U_{CE}$ ~~$\sum NICs\_U_{CE}$~~) and anticyclonic eddies ($NICs\_U_{AE}$ ~~$\sum NICs\_U_{CE}$~~) . Both values of $NICs\_U_{CE}$ ~~$\sum NICs\_U_{AE}$~~ and $NICs\_U_{AE}$ ~~$\sum NICs\_U_{CE}$~~ are larger for higher eddy strengths, particularly for the anticyclonic eddies. For the $|SLA_c|$ values equal to 0.13 m, values of $NICs\_U_{AE}$ ~~$\sum NICs\_U_{AE}$~~ and $NICs\_U_{CE}$ ~~$\sum NICs\_U_{CE}$~~ are about 2.10×10^{-3}~~0.019~~ m s^{-1} and about 3.15×10^{-4}~~0.003~~ m s^{-1}. The averaged speeds of the converted NICs increase with the $|SLA_c|$ value, particularly for the anticyclonic eddies. For $|SLA_c|$ = 1.02 m, the averaged speeds of the transferred NICs are ~3.11×10^{-2}~~0.280~~ m s^{-1} and ~1.94×10^{-2}~~0.175~~ m s^{-1} for the anticyclonic and cyclonic eddies respectively, which are approximatively ~~14.74~~ 15 times and approximatively 62 ~~58.33~~ times larger than the counterparts at $|SLA_c|$ = 0.13 m. As the geostrophic strain field is relatively stronger at the eddy edge, the average speeds of the converted NICs at the mesoscale eddy edge are larger than that at the mesoscale eddy center.
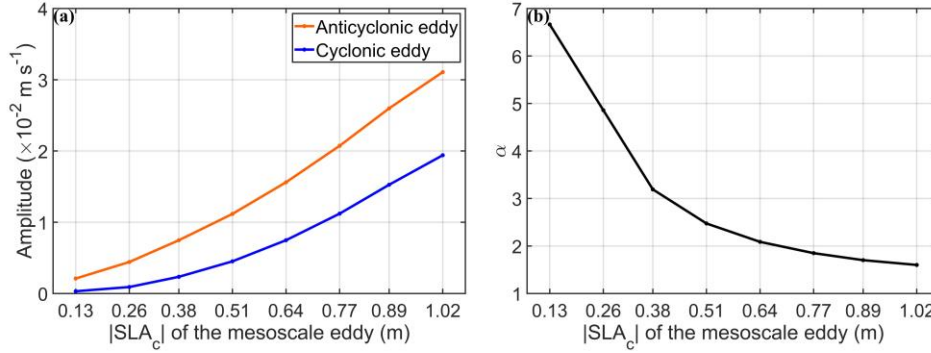
Figure 9. (a) ~~Sum of a~~Averaged speeds of transferred NICs at 9 fixed locations P1-P9 as a function of the strengths ($|SLA_c|$ of the mesoscale eddy) of the anticyclonic eddy (orange line) and cyclonic eddy (blue line). (b) The α value as a function of the eddy strengths ($|SLA_c|$ of the mesoscale eddy). The mesoscale eddy moves westward at the speed of 8 cm s^{-1}. The speed of the cyclonically rotating wind speed at the inertial frequency is set to 13 m s^{-1}.

The α value also varies with the mesoscale eddy strength (Fig. 9b). The α value decreases significantly from about 6.66 to 1.60 for the $|SLA_c|$ values in the range of 0.13 and 1.02 m. As mentioned above, cyclonic eddies have limited ability in transferring their kinetic energy to NICs, which differs significantly from anticyclonic eddies. However, stronger cyclonic eddies with more eddy energy provide the more favorable condition for the energy transfer, which can narrow the difference in the near-inertial energy transfer induced by anticyclonic eddies and cyclonic eddies. Furthermore, stronger geostrophic currents lead to stronger geostrophic strain field which can generate stronger NICs.

5.6 Relative Vorticity and Strain

As mentioned above, the anticyclonic eddies in the SML are more efficient than cyclonic eddies for transferring kinetic energy to NICs, which can be explained by the relative vorticity of the background flow (ζ) defined in Eq. (1). In numerical experiments, the direction of the energy transfer is bidirectional, but primarily positive, that is, from mesoscale eddies to NICs. For cyclonic eddies, the direction of the energy transfer is from the NICs to the cyclonic eddy under cyclonically rotating winds at frequencies of $0.25f$, $0.75f$ and $1.25f$ and anticyclonically rotating

601 winds at frequency range of -1.15f to -0.75f. When the frequencies of anticyclonically rotating
602 winds are range from -1.5f to -0.9f, the energy transfer is also negative in the anticyclonic eddy.
603 The α value is more than 1.0 for about 87% of these experiments, which indicates that the
604 transferred near-inertial energy is larger in anticyclonic eddies than cyclonic eddies.

605   In addition to the relative vorticity and translational speed of a mesoscale eddy, the normal
606 strain and shear strain of the background flow can also affect the energy transfer between the
607 mesoscale eddy and NICs in the SML. Jing et al. (2017) proposed a method to calculate the rate
608 of energy transfer from background mesoscale eddies to wind-induced NICs. Following Jing et al.
609 (2017), the energy transfer rate (ε) between the NICs and the mesoscale eddy in the SML is given
610 as

$$\varepsilon = -\rho H_{mix}\left(uuU_x + uvU_y + uvU_x + vvV_y\right), \tag{26}$$

612 where u and v are respectively the zonal and meridional components of the near-inertial current
613 velocity reproduced by the modified slab model, and subscripts x and y in U and V represent partial
614 derivatives. The positive ε mean the energy transfer from the mesoscale eddy to the NICs, and the
615 negative ε indicates the backward energy cascade. In the numerical experiments, the NICs can be
616 generated directly by the cyclonic winds, and the wind-induced NICs can further interact with the
617 mesoscale eddy and transfer the near-inertial energy from the mesoscale eddy to the NICs when
618 the mesoscale eddy passed by the nine locations P1-P9. Therefore, we also calculate the energy
619 transfer rate and Okubo-Weiss parameter at the nine fixed locations P1-P9 in the sensitivity
620 experiments ExpA3, ExpC1-C9 and ExpD1-D16, which are under the same wind conditions.

621   When the Okubo-Weiss parameters (strains) are negative, the energy transfer rate decreases
622 as the Okubo-Weiss parameter (strain) increases (Fig. 10). However, when the Okubo-Weiss
623 parameters (strains) are positive, the energy transfer rate shows an elevated trend with the increase
624 of the Okubo-Weiss parameter (strain). Based on limited sensitivity studies, we found the relative
625 vorticity and the strain of the mesoscale eddy both have an influence on the near-inertial energy
626 transferred by interactions between mesoscale eddies and NICs.
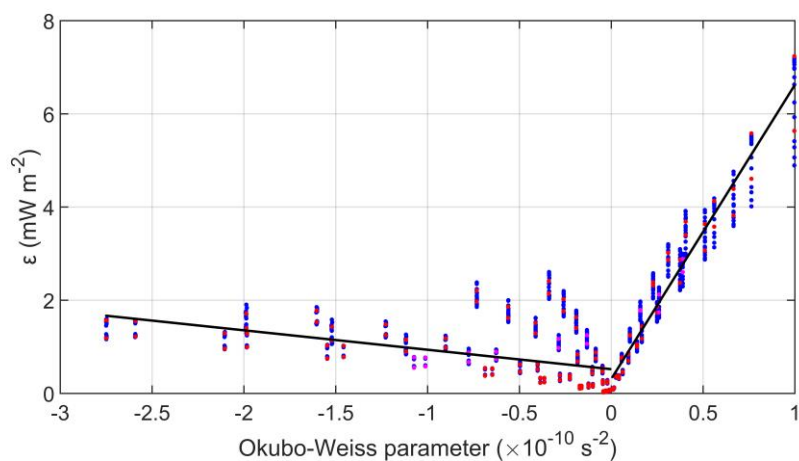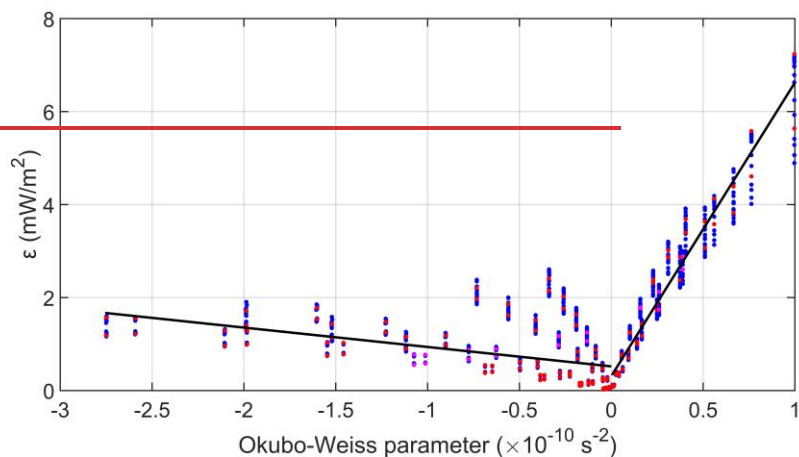
627
628

629

Figure 10. Scatterplot between the energy transfer rate and the Okubo-Weiss parameter. Purple, blue and red dots respectively represent ExpA3, ExpC1-9 and ExpD1-16. The left (right) black line is the linear fitting line when the Okubo-Weiss parameters are negative (positive).

28

6 Theoretical Analyses

6.1 Solutions in the Frequency Domain

To gain better understanding of the role of the relative vorticity in the background flow for anticyclonic eddies to be significantly more efficient than the cyclonic eddies in transferring their kinetic energy to NICs, we examine analytically the effect of the relative vorticity in the frequency domain solution of the modified slab model.

The modified slab model can be written in the tensor form:

$$\frac{\partial}{\partial t}\begin{Bmatrix} u \\ v \end{Bmatrix} + \begin{bmatrix} a_1 & b_1 \\ a_2 & b_2 \end{bmatrix}\begin{Bmatrix} u \\ v \end{Bmatrix} = \begin{Bmatrix} c_1 \\ c_2 \end{Bmatrix}, \tag{27}$$

where, $a_1 = U_x + r$, $a_2 = V_x + f$, $b_1 = U_y - f$, $b_2 = V_y + r$, $c_1 = \tau_x/\rho H_{mix}$ and $c_2 = \tau_y/\rho H_{mix}$. Under the steady winds, the NICs produced by the original slab model are zero, therefore the NICs produced by the modified slab model directly represent the near-inertial energy converted between mesoscale eddies and NICs. For simplicity, we consider the steady wind forcing to directly eliminate the wind-induced NICs here. In the case of steady winds, we use the Fourier transform to translate the modified slab model from the time domain into the frequency domain:

$$\begin{bmatrix} a_1 + i\omega & b_1 \\ a_2 & b_2 + i\omega \end{bmatrix}\begin{Bmatrix} \tilde{u} \\ \tilde{v} \end{Bmatrix} = \begin{Bmatrix} \tilde{c}_1 \\ \tilde{c}_2 \end{Bmatrix}, \tag{28}$$

where ω is the frequency and variables with a tilde represent the values after Fourier transform.

Assuming the mesoscale eddy is in an almost steady state during an inertial period (Jing et al. 2017), the analytical solution for the zonal and meridional components of NICs in the frequency domain can be written as

$$\tilde{u} = \frac{(b_2+i\omega)\cdot 2\cdot\pi\cdot c_1\cdot\delta(\omega)-b_1\cdot 2\cdot\pi\cdot c_2\cdot\delta(\omega)}{(a_1+i\omega)(b_2+i\omega)-a_2 b_1}, \tag{29}$$

$$\tilde{v} = \frac{(a_1+i\omega)\cdot 2\cdot\pi\cdot c_2\cdot\delta(\omega)-a_2\cdot 2\cdot\pi\cdot c_1\cdot\delta(\omega)}{(a_1+i\omega)(b_2+i\omega)-a_2 b_1}, \tag{30}$$

where $\delta(\omega)$ is the Dirac Delta function.

Based on Perceval's theorem, the energy of NICs is the same in both the time and frequency domains:

$$\frac{1}{T}\int |U(t)|^2 dt = \int |U(\omega)|^2 d\omega, \tag{31}$$

where T is the total period.

29

The time-mean near-inertial kinetic energy $\overline{U_{NIW_s}}^2$ in the time domain can be written as

$$\overline{U_{NIW_s}}^2 = \overline{u^2} + \overline{v^2}, \tag{32}$$

$$\overline{u^2} = \int \frac{\left((b_2 c_1 - b_1 c_2)^2 + \omega^2 c_1{}^2\right) \cdot \left((2 \cdot \pi \cdot \delta(\omega))^2\right)}{(a_2 b_1 - a_1 b_2 + \omega^2)^2 + \omega^2 (a_1 + b_2)^2} \cdot d\omega, \tag{33}$$

$$\overline{v^2} = \int \frac{\left((a_1 c_2 - a_2 c_1)^2 + \omega^2 c_2{}^2\right) \cdot \left((2 \cdot \pi \cdot \delta(\omega))^2\right)}{(a_2 b_1 - a_1 b_2 + \omega^2)^2 + \omega^2 (a_1 + b_2)^2} \cdot d\omega. \tag{34}$$

For a unidirectional laterally sheared geostrophic flow and the southwestward wind, U=0, V=V(x), $c_1 < 0$ and $c_2 < 0$. Substitution of $a_1 = r$, $a_2 = \zeta + f$, $b_1 = -f$ and $b_2 = r$ into Eq. (33) and Eq. (34) yields

$$\overline{u^2} = \int \frac{\left((rc_1 + fc_2)^2 + \omega^2 c_1{}^2\right)\left((2 \cdot \pi \cdot \delta(\omega))^2\right)}{\left(r^2 - \omega^2 + f(\zeta + f)\right)^2 + 4\omega^2 r^2} d\omega, \tag{35}$$

$$\overline{v^2} = \int \frac{\left((rc_2 - (\zeta + f)c_1)^2 + \omega^2 c_2{}^2\right)\left((2 \cdot \pi \cdot \delta(\omega))^2\right)}{\left(r^2 - \omega^2 + f(\zeta + f)\right)^2 + 4\omega^2 r^2} d\omega. \tag{36}$$

Since the relative vorticity is negative in anticyclonic eddies, the denominator term for $\overline{u^2}$ in Eq. (35) is less than the value with positive relative vorticity. Therefore, the value of $\overline{u^2}$ is greater in anticyclonic eddies than in cyclonic eddies. For the positive relative vorticity, the numerator term of $\overline{v^2}$ is smaller and the denominator term in Eq. (36) becomes larger than the case of negative vorticity. This indicates that $\overline{v^2}$ is more elevated in the anticyclonic eddies. Since both $\overline{u^2}$ and $\overline{v^2}$ are elevated when the relative vorticity is negative than counterparts with the positive relative vorticity, anticyclonic eddies can transfer more near-inertial energy than cyclonic eddies.

6.2 Analytical Solution

An analytical solution based on the modified slab model is considered here to demonstrate that mesoscale eddies can transfer more near-inertial energy for stronger winds. The modified slab model cane be written as

$$\frac{\partial u}{\partial t} + a_1 u + b_1 v = c_1, \tag{37}$$

$$\frac{\partial v}{\partial t} + a_2 u + b_2 v = c_2, \tag{38}$$

where, $a_1 = U_x + r$, $a_2 = V_x + f$, $b_1 = U_y - f$, $b_2 = V_y + r$, $c_1 = \tau_x / \rho H_{mix}$, $c_2 = \tau_y / \rho H_{mix}$, $\tau_x = A\cos ft$ and $\tau_y = A\sin ft$.

For the cyclonic wind, substitution of Eq. (37) into Eq. (38) yields

$$\frac{\partial^2 u}{\partial t^2} + (a_1 + b_2)\frac{\partial u}{\partial t} + (a_1 b_2 - a_2 b_1)u = b_2 c_1 - (f + b_1)c_2 \tag{39}$$

30

$$\Delta = (a_1 + b_2)^2 - 4(a_1 b_2 - a_2 b_1). \tag{40}$$

The analytical solutions of the current to the modified slab model are

$$u_{Modified} = e^{\gamma t}(Q_1 cos\beta t + Q_2 sin\beta t) + Q_3 cosft + Q_4 sinft, \tag{41}$$

$$v_{Modified} = \frac{1}{b_1}(c_1 - e^{\gamma t}(a_1 + \gamma)(Q_1 cos\beta t + Q_2 sin\beta t)$$

$$-e^{\gamma t}\beta(Q_2 cos\beta t - Q_1 sin\beta t) + (fQ_3 - a_1 Q_4)sinft - (fQ_4 + a_1 Q_3)cosft), \tag{42}$$

where

$$\gamma = -\frac{a_1 + b_2}{2}, \tag{43}$$

$$\beta = \frac{\sqrt{-\Delta}}{2}, \tag{44}$$

$$Q_1 = -Q_3, \tag{45}$$

$$Q_2 = \frac{c_1 + \gamma Q_3 - fQ_4}{\beta}, \tag{46}$$

$$Q_3 = \frac{Ab_2(a_1 b_2 - a_2 b_1 - f^2) + A(f + b_1)(f a_1 + f b_2)}{\rho H_{mix}((a_1 b_2 - a_2 b_1 - f^2)^2 + (f a_1 + f b_2)^2)}, \tag{47}$$

$$Q_4 = \frac{\rho H_{mix} Q_3 (f a_1 + f b_2) - A(f + b_1)}{\rho H_{mix}(a_1 b_2 - a_2 b_1 - f^2)}. \tag{48}$$

Increasing the wind stress c_1 and c_2 by a factor of n named c_1' and c_2' yields

$$c_1' = nc_1 = \frac{n\tau_x}{\rho H_{mix}} = \frac{nAcosft}{\rho H_{mix}}, \tag{49}$$

$$c_2' = nc_2 = \frac{n\tau_y}{\rho H_{mix}} = \frac{nAsinft}{\rho H_{mix}}. \tag{50}$$

Substitution of c_1' and c_2' into Q_3 and Q_4 yields

$$Q_3' = \frac{nAb_2(a_1 b_2 - a_2 b_1 - f^2) + nA(f + b_1)(f a_1 + f b_2)}{\rho H_{mix}((a_1 b_2 - a_2 b_1 - f^2)^2 + (f a_1 + f b_2)^2)} = nQ_3, \tag{51}$$

$$Q_4' = \frac{\rho H_{mix} nQ_3 (f a_1 + f b_2) - nA(f + b_1)}{\rho H_{mix}(a_1 b_2 - a_2 b_1 - f^2)} = nQ_4. \tag{52}$$

Substitution of Q_3 and Q_4 into Q_1 and Q_2 yields

$$Q_1' = -nQ_3 = nQ_1, \tag{53}$$

$$Q_2' = \frac{nc_1 + \gamma nQ_3 - fnQ_4}{\beta} = nQ_2. \tag{54}$$

Therefore, the current with the increased wind stress to the modified slab model is given as

$$u_{Modified}' = nu_{Modified}, \tag{55}$$

$$v_{Modified}' = nv_{Modified}. \tag{56}$$

The analytical solution of the current to the original slab model is

$$U_{Original} = \frac{Ae^{ift}}{\rho H_{mix}(if + r)} + \left(\left(\frac{Ae^{-(if+r)t}}{\rho H_{mix}(if + r)} \right) \left(\frac{if}{2if + r} \right) \left(1 - e^{(2if + r)t} \right) \right) - \frac{Ae^{-(if+r)t}}{\rho H_{mix}(if + r)}. \tag{57}$$

31

711   Therefore, the current with the increased wind stress to the original slab model is given as

712
$$U_{Original}' = nU_{Original}.\qquad(58)$$

713   The above analytical solutions demonstrate that when the wind stress increases by n times,

714 the current speeds simulated by the modified and original slab models both increase by n times.

715 The differences in the average speeds of NICs between the modified and original model represent

716 the transferred near-inertial energy by the interaction between mesoscale eddies and near-inertial

717 motions (Eq. (22) and (23)). As the NICs are the component of the total currents in the near-inertial

718 frequency band, the transferred near-inertial energy in the mesoscale eddies also increases by a

719 factor of n times when the wind stress is multiplied by n times. This feature is consistent with our

720 sensitivity experiments in Sect. 5.

721 **7 Summary and Discussion**

722   Analysis of in situ current observations at two offshore ADCP mooring sites in the northern

723 South China Sea (nSCS) demonstrated that relatively strong near-inertial currents (NICs) occurred

724 during certain periods of nearly steady winds in the lower part of the ocean surface mixed layer

725 (SML). The NICs produced by the original slab model are significantly larger than the observations,

726 indicating other important processes operating over the area. We followed Welle (1982) and Jing

727 et al. (2017) and used a modified slab model in this study by including contributions from the

728 background geostrophic currents. Using the surface geostrophic currents inferred from the satellite

729 sea level data and assuming the geostrophic currents in the SML is vertically uniform, we found

730 that the modified slab model performs significantly better than the original slab model in

731 reproducing the observed NICs at two ADCP mooring sites in the nSCS. Examinations of

732 observations and numerical results produced by the modified and original slab models revealed

733 the occurrence of the energy exchange between the mesoscale eddies and the NICs. Based on the

734 energy budget analysis for NICs during the observational period, the difference of the near-inertial

735 wind power input between the original slab model and the modified slab model is the same order

736 as the energy transfer rate (Eq. 26). This also indicates the importance of the near-inertial energy

737 transfer induced by the interaction between mesoscale eddies and NICs in the SML during the

738 observational period.

739   The modified slab model and original slab model were then used to examine sensitivity to

740 winds and eddy parameters with idealized mesoscale eddies under cyclonic winds. Both cyclonic

32

741 and anticyclonic mesoscale eddies were considered, using the universal eddy structure suggested
742 by Zhang et al. (2013). One of our major findings is that anticyclone eddies can transfer more
743 kinetic energy to NICs than cyclonic eddies. Idealized experiments show that induced NICs speed
744 in anticyclonic eddies can reach over 6 times the speed in cyclonic eddies. We also found that the
745 energy transfer rate is related to the Okubo-Weiss parameter. When the Okubo-Weiss parameter
746 is positive, the energy transfer rate is elevated with the larger Okubo-Weiss parameter.

747   Analyses of model results in ~~196~~ 226 numerical experiments using the modified slab model
748 demonstrated that there exists bidirectional energy transfer between mesoscale eddies and NICs.
749 The direction of the energy transfer is primarily from mesoscale eddies to NICs. When the cyclonic
750 winds rotate at frequencies of $0.25f$, $0.75f$ and $1.25f$ and the anticyclonic winds rotate at
751 frequencies ranging from $-1.15f$ to $-0.75f$, the direction of the energy transfer is negative in the
752 cyclonic eddy, that is, from NICs to cyclonic eddies. Under anticyclonically rotating winds at the
753 frequency range of $-1.5f$ to $-0.9f$, the negative energy transfer also occurs in the anticyclonic eddy.
754 The NICs transferred from mesoscale eddies are stronger for higher wind speeds, faster
755 translational speeds and stronger strengths of mesoscale eddies. When the wind stress increases by
756 a factor of n times, the amplitudes of the converted NICs are also multiplied by n times. The NICs
757 transferred in mesoscale eddies by the interactions between mesoscale eddies and NICs are
758 stronger for higher translational speeds of anticyclonic eddies. At the translational speeds of 11
759 cm s^{-1}, the ratios of the amplitudes of the converted NICs by anticyclonic eddies to that transferred
760 by cyclonic eddies reach maximum values.

761   For analytical considerations, the modified slab model was transferred from the time domain
762 to the frequency domain using the Fourier transform. Using Parseval's theorem, we derived the
763 time-mean value of the induced NICs. The analytical expression was used to demonstrate that, for
764 the negative relative vorticity, i.e., such as within an anticyclonic eddy, the transferred NICs are
765 larger in an anticyclonic eddy than a cyclonic eddy. The analytical solution under the cyclonic
766 winds also demonstrated that the NICs transferred by mesoscale eddies increase linearly with the
767 wind stress. These analytical results are consistent with the results produced by the modified and
768 original slab models.

769   We also conducted the same set of numerical experiments using steady winds in both constant
770 speeds and direction and model results in the steady winds are not presented here due to the page

33

limit. Our main findings on the energy transfer between mesoscale eddies and NICs in these experiments with the steady winds are the same as the results using the rotating winds.

This study suggests that there is bidirectional energy transfer between mesoscale eddies and NICs in the SML, of which the mechanism and influence factors are further explored by idealized simulations. Our findings can further contribute to the understanding of the energy budget in the global ocean and the ocean response to the climate change. In order to examine major physical processes affecting the NICs generated by the mesoscale eddies and quantify their influence on turbulent mixing in the deeper ocean, further studies are needed using a three-dimensional ocean circulation model.

Data availability

All the data can be obtained by contacting the authors.

Competing interests

The authors declare that they have no conflict of interest.

Author contributions

Yu Zhang: Writing - original draft, Visualization, Validation, Software, Methodology, Investigation, Data curation, Conceptualization.

Jintao Gu: Writing - review & editing, Visualization, Methodology, Conceptualization.

Shengli Chen: Writing - review & editing, Project administration, Methodology, Funding acquisition, Data curation.

Jianyu Hu: Writing - review & editing, Data curation.

Jinyu Sheng: Writing - review & editing.

Jiuxing Xing: Writing - review & editing, Supervision.

References

Alford, M. H.: Improved global maps and 54-year history of wind-work on ocean inertial motions, Geophys. Res. Lett., 30(8), https://doi.org/10.1029/2002GL016614, 2003.

Alford, M. H., MacKinnon, J. A., & Simmons, H. L.: Near-inertial internal gravity waves in the ocean, Ann. Rev. Mar. Sci., 8, 95–123, https://doi.org/10.1146/annurev-marine-010814-015746, 2016.

Barkan, R., Srinivasan, K., & Yang, L.: Oceanic mesoscale eddy depletion catalyzed by internal waves, Geophys. Res. Lett., 48(18), e2021GL094376, https://doi.org/10.1002/essoar.10507068.1, 2021.

Boyer, T.P., O.K. Baranova, C. Coleman, H.E. Garcia, A. Grodsky, R.A. Locarnini, A.V. Mishonov, C.R. Paver, J.R. Reagan, D. Seidov, I.V. Smolyar, K.W. Weathers, & M.M. Zweng.: NOAA Atlas NESDIS 87, World Ocean Database 2018 [Dataset], https://www.ncei.noaa.gov/access/world-ocean-atlas-2018/, 2019.

Bühler, O., & McIntyre, M. E.: Wave capture and wave–vortex duality, J. Fluid Mech., 534, 67–95. https://doi.org/10.1017/S0022112005004374, 2005.

Chelton, D. B., Schlax, M. G., & Samelson, R. M.: Global observations of nonlinear mesoscale eddies, Prog. Oceanogr., 91(2), 167–216, https://doi.org/10.1016/j.pocean.2011.01.002, 2011.

Chen, S.: OSF, The Current Observation Data (S2 and S3) in the Mixed Layer [Dataset], https://doi.org/osf.io/r9kyz, 2023.

Chen, S., J. Polton, Hu, J., & Xing, J.: Local inertial oscillations in the surface ocean generated by time-varying winds, Ocean Dyn., 65, 1633–1641, https://doi.org/10.1007/s10236-015-0899-6, 2015a.

Chen, S., Hu, J. & J. A. Polton.: Features of near-inertial motions observed on the northern South China Sea shelf during the passage of two typhoons, Acta Oceanol. Sin., 34, 38–43, https://doi.org/10.1007/s13131-015-0594-y, 2015b.

Chen, S., J. A. Polton, Hu, J., & Xing, J.: Thermocline bulk shear analysis in the northern North Sea, Ocean Dyn., 66, 499–508, https://doi.org/10.1007/s10236-016-0933-3, 2016.

Chen, S., Chen, D. & Xing, J.: A study on some basic features of inertial oscillations and near-inertial internal waves, Ocean Sci., 13, 829–836, https://doi.org/10.5194/os-2017-33, 2017.

Chen, G., Xue, H., & Wang, D.: Observed near-inertial kinetic energy in the northwestern South China Sea, J. Geophys. Res.-Oceans, 118(10), 4965–4977, https://doi.org/10.5194/os-2017-33, 2013.

831 Copernicus Climate Change Service, Climate Data Store.: Sea level gridded data from satellite
832   observations for the global ocean from 1993 to present [Dataset],
833   https://doi.org/10.24381/cds.4c328c78, 2018.

834 D'Asaro E. A.: The energy flux from the wind to near-inertial motions in the surface mixed layer,
835   J. Phys. Oceanogr., 15(8), 1043–1059, https://doi.org/10.1175/1520-
836   0485(1985)015<1043:tefftw>2.0.co;2, 1985.

837 D'Asaro, E. A., Eriksen C. C., & Levine M. D.: Upper-ocean inertial currents forced by a strong
838   storm. Part I: data and comparisons with linear theory, J. Phys. Oceanogr., 25(11), 2909–
839   2936, https://doi.org/10.1175/1520-0485(1995)025<2909:uoicfb>2.0.co;2, 1995.

840 Elipot, S., Lumpkin, R., & Prieto, G.: Modification of inertial oscillations by the mesoscale eddy
841   field, J. Geophys. Res.-Oceans, 115(C9), https://doi.org/10.1029/2009jc005679, 2010.

842 Fer, I., Bosse, A., Ferron, B., & Bouruet-Aubertot, P.: The dissipation of kinetic energy in the
843   Lofoten Basin Eddy, J. Phys. Oceanogr., 48(6), 1299-1316, https://doi.org/10.1175/JPO-
844   D-17-0244.1, 2018.

845 Ferrari, R., & Wunsch, C.: Ocean circulation kinetic energy: Reservoirs, sources, and sinks, Annu.
846   Rev. Fluid Mech., 41, 253–282, https://doi.org/10.1146/annurev.fluid.40.111406.102139,
847   2009.

848 Ford, R., McIntyre, M. E., & Norton, W. A.: Balance and the slow quasimanifold: some explicit
849   results, J. Atmos. Sci., 57(9), 1236–1254, https://doi.org/10.1175/1520-
850   0469(2000)057<1236:BATSQS>2.0.CO;2, 2000.

851 Garrett, C.: What is the ''near-inertial'' band and why is it different from the rest of the internal
852   wave spectrum?, J. Phys. Oceanogr., 31, 962–971, https://doi.org/10.1175/1520-
853   0485(2001)031,0962: WITNIB.2.0.CO;2, 2001.

854 Gill A.: On the Behavior of Internal Waves in the Wakes of Storms, J. Phys. Oceanogr., 14(7),
855   1129–1151, https://doi.org/10.1175/1520-0485(1984)014<1129:otboiw>2.0.co;2, 1984.

856 Greatbatch, R. J.: On the response of the ocean to a travelling storm: Parameters and scales, J.
857   Phys. Oceanogr., 14, 59–78, https://doi.org/10.1175/1520-
858   0485(1984)014,0059:OTROTO.2.0.CO;2, 1984.

859 Hersbach, H., Bell, B., Berrisford, P., Biavati, G., Horányi, A., Muñoz Sabater, J., Nicolas, J.,
860   Peubey, C., Radu, R., Rozum, I., Schepers, D., Simmons, A., Soci, C., Dee, D., & Thépaut,
861   J-N.: Copernicus Climate Change Service (C3S) Climate Data Store (CDS), ERA5 hourly
862   data on single levels from 1940 to present [Dataset],
863   https://doi.org/10.24381/cds.adbb2d47, 2023.

864 Jaimes, B., & Shay, LK.: Near-Inertial Wave Wake of Hurricanes Katrina and Ritaover Mesoscale
865   Oceanic Eddies, J. Phys. Oceanogr., 40(6), 1320–1337,
866   https://doi.org/10.1175/2010JPO4309.1, 2010.

867 Jing, Z., Wu, L., & Ma, X.: Sensitivity of near-inertial internal waves to spatial interpolations of
868   wind stress in ocean generation circulation models, Ocean Modell., 99, 15–21,
869   https://doi.org/10.1016/j.ocemod.2015.12.006, 2016.

870 Jing, Z., Wu, L., & Ma, X.: Energy exchange between the mesoscale oceanic eddies and wind-
871   forced near-inertial oscillations, J. Phys. Oceanogr., 47(3), 721–733,
872   https://doi.org/10.1175/JPO-D-16-0214.1, 2017.

Jing, Z., Chang, P., DiMarco, S.F., & Wu, L.: Observed energy exchange between low-frequency flows and internal waves in the Gulf of Mexico, J. Phys. Oceanogr., 48, 995–1008, https://doi.org/10.1175/JPO-D-17-0263.1, 2018.

Jochum, M., Briegleb, B., Danabasoglu, G., Large., W, Norton, N., Jayne, S., Alford, M., & Bryan, F.: The impact of oceanic near-inertial waves on climate, J. Clim., 26, 2833–2844, https://doi.org/10.1175/JCLI-D-12-00181.1, 2013.

Kunze, E.: Near-inertial wave propagation in geostrophic shear, J. Phys. Oceanogr., 15(5), 544–565, https://doi.org/10.1175/1520-0485(1985)015<0544:NIWPIG>2.0.CO;2, 1985.

Lelong, M. P., Cuypers, Y., & Bouruet-Aubertot, P.: Near-inertial energy propagation inside a Mediterranean anticyclonic eddy, J. Phys. Oceanogr., 50(8), 2271-2288, https://doi.org/10.1175/JPO-D-19-0211.1, 2020.

Liu, G., Chen, Z., Lu, H., Liu, Z., Zhang, Q., He, Q., He, Y., Xu, J., Gong, Y., & Cai, S.: Energy transfer between mesoscale eddies and near-inertial waves from surface drifter observations, Geophys. Res. Lett., 50, e2023GL104729, https://doi.org/10.1029/2023GL104729, 2023.

McWilliams, J. C.: Submesoscale currents in the ocean, Proc. R. Soc. A., 472(2189), 20160117, https://doi.org/10.1098/rspa.2016.0117, 2016.

Mooers, C. N.: Several effects of a baroclinic current on the cross-stream propagation of inertial-internal waves, Geophys. Fluid Dyn., 6(3), 245–275, https://doi.org/10.1080/03091927509365797, 1975.

Muller, P.: On the diffusion of momentum and mass by internal gravity waves, J. Fluid Mech., 77(4), 789–823, https://doi.org/10.1017/S0022112076002899, 1976.

Munk, W., & Wunsch, C.: Abyssal recipes II: Energetics of tidal and wind mixing, Deep-Sea Res. Pt. I, 45, 1977–2010, https://doi.org/10.1016/S0967-0637(98)00070-3, 1998.

Noh, S., & Nam, S.: Observations of enhanced internal waves in an area of strong mesoscale variability in the southwestern East Sea (Japan Sea), Sci. Rep., 10, 9068, https://doi.org/10.1038/s41598-020-65751-1, 2020.

Oey, L. Y., Ezer, T., &Wang, D. P.: Loop current warming by hurricane Wilma, Geophys. Res. Lett., 33(8), L08613, https://doi.org/ 10.1029/2006GL025873, 2006.

Okubo, A.: Horizontal dispersion of floatable particles in the vicinity of velocity singularities such as convergences, Deep. Sea Res. Oceanogr. Abstr., 17(3), 445–454, https://doi.org/10.1016/0011-7471(70)90059-8, 1970.

Paduan, J. D., Szoeke, R. A., & Weller, R. A.: Inertial oscillations in the upper ocean during the Mixed Layer Dynamics Experiment (MILDEX), J. Geophys. Res., 94, 4835–4842, https://doi.org/10.1029/JC094iC04p04835, 1989.

Perkins, H.: Observed effect of an eddy on inertial oscillations, Deep. Sea Res. Oceanogr. Abstr., 23(11), 1037–1042, https://doi.org/10.1016/0011-7471(76)90879-2, 1976.

Pollard, R. T., & Millard, R. C.: Comparison between observed and simulated wind-generated inertial oscillations, Deep. Sea Res. Oceanogr. Abstr., 17, 813–816, https://doi.org/10.1016/0011-7471(70)90043-4, 1970.

Price, J. F., Weller, R. A., & Pinkel, R.: Diurnal cycling: Observations and models of the upper ocean response to diurnal heating, cooling, and wind mixing, J. Geophys. Res., 91, 8411–8427, https://doi.org/10.1029/JC091iC07p08411, 1986.

Shu, Y., Wang, Q., & Zu, T.: Progress on shelf and slope circulation in the northern South China Sea, Sci. China Earth Sci., 61, 560–571, https://doi.org/10.1007/s11430-017-9152-y, 2018.

Sun, Z., Hu, J., & Zheng, Q.: Strong near-inertial oscillations in geostrophic shear in the northern South China Sea, J. Oceanogr., 67(4), 377–384, https://doi.org/ 10.1007/s10872-011-0038-z, 2011.

Thomas, L. N.: On the effects of frontogenetic strain on symmetric instability and inertia–gravity waves, J. Fluid Mech., 711, 620–640, https://doi.org/ 10.1017/jfm.2012.416, 2012.

Thomas, L. N.: On the modifications of near-inertial waves at fronts: Implications for energy transfer across scales, Ocean Dyn., 67(10), 1–16, https://doi.org/10.1007/s10236-017-1088-6, 2017.

van Meurs, P.: Interactions between near-inertial mixed layer currents and the mesoscale: the importance of spatial variabilities in the vorticity field, J. Phys. Oceanogr., 28(7), 1363–1388, https://doi.org/10.1175/1520-0485(1998)0282.0.CO;2, 1998.

Vanneste, J.: Balance and spontaneous wave generation in geophysical flows, Annu. Rev. Fluid Mech., 45, 147–172, https://doi.org/10.1146/annurev-fluid-011212-140730, 2013.

Wang, Y., Guan, S., Zhang, Z., Zhou, C., Xu, X., Guo, C., Zhao, W. & Tian, J.: Observations of Parametric Subharmonic Instability of Diurnal Internal Tides in the Northwest Pacific, J. Phys. Oceanogr., 54(3), 849-870, https://doi.org/10.1175/JPO-D-23-0055.1, 2024.

Weller, R. A.: The relation of near-inertial motions observed in the mixed layer during the JASIN (1978) experiment to the local wind stress and to the quasi-geostrophic flow field, J. Phys. Oceanogr., 12, 1122–1136, https://doi.org/10.1175/1520-0485(1982)0122.0.CO;2, 1982.

Wei, Z., Xue, H., & Qin, H.: Using idealized numerical experiment to study an eddy colliding with an island, J. Trop. Oceanogr., 36(4), 35-47, https://doi.org/10.11978/2016118, 2017.

Whalen, C. B., Lavergne, C. D., Garabato, A. C. N., Klymak, J. M., & Sheen, K. L.: Internal wave-driven mixing: Governing processes and consequences for climate, Nat Rev Earth Environ, 1(11), 606–621, https://doi.org/10.1038/s43017-020-0097-z, 2020.

Whitt, D. B., & L. N. Thomas.: Resonant generation and energetics of wind-forced near-inertial motions in a geostrophic flow, J. Phys. Oceanogr., 45, 181–208, https://doi.org/10.1175/JPO-D-14-0168.1, 2015.

Wunsch, C., & Ferrari, R.: Vertical mixing, energy and the general circulation of the oceans, Annu. Rev. Fluid Mech., 36, 281–314, https://doi.org/10.1146/annurev.fluid.36.050802.122121, 2004.

Xie, J., & Vanneste, J.: A generalised-Lagrangian-mean model of the interactions between near-inertial waves and mean flow, J. Fluid Mech., 774, 143–169, https://doi.org/10.1017/jfm.2015.251, 2015.

Young, W. R., & Jelloul, M. B.: Propagation of near-inertial oscillations through a geostrophic flow, J. Mar. Res., 55(4), 735–766, https://doi.org/10.1357/0022240973224283, 1997.

Zhai, X., Greatbatch, R. & Zhao, J.: Enhanced vertical propagation of storm-induced near-inertial energy in an eddying ocean channel, Geophys. Res. Lett., 32(18), L18602, https://doi.org/10.1029/2005GL023643, 2005.

Zhai, X., Greatbatch, R. J. & Eden, C.: Spreading of near-inertial energy in a 1/12° model of the North Atlantic Ocean, Geophys. Res. Lett., 34(10), 421–428, https://doi.org/10.1029/2007GL029895, 2007.

959   Zhang, Z., Zhang, Y., & Wang, W.: Universal structure of mesoscale eddies in the ocean, Geophys.
960   Res. Lett., 40(14), 3677–3681, https://doi.org/10.1002/grl.50736, 2013.